RESEARCH ARTICLE - APPLICATION

Effect of heated-air blanket on the dispersion of squames in an operating room

X. He[1] | S. Karra[1] | P. Pakseresht[1] | S. V. Apte[1] | S. Elghobashi[2]

[1]Department of Mechanical Engineering, Oregon State University, Corvallis, OR, USA

[2]Mechanical and Aerospace Engineering, The Henri Samueli School of Engineering, University of California, Irvine, CA, USA

Correspondence
Sourabh V. Apte, Department of Mechanical Engineering, Oregon State University, Corvallis, OR, USA.
Email: Sourabh.Apte@oregonstate.edu

Abstract

High-fidelity, predictive fluid flow simulations of the interactions between the rising thermal plumes from forced air warming blower and the ultra-clean ventilation air in an operating room (OR) are conducted to explore whether this complex flow can impact the dispersion of squames to the surgical site. A large-eddy simulation, accurately capturing the spatiotemporal evolution of the flow in 3 dimensions together with the trajectories of squames, is performed for a realistic OR consisting of an operating table (OT), side tables, surgical lamps, medical staff, and a patient. Two cases are studied with blower-off and blower-on together with Lagrangian trajectories of 3 million squames initially placed on the floor surrounding the OT. The large-eddy simulation results show that with the blower-off, squames are quickly transported by the ventilation air away from the table and towards the exit grilles. In contrast, with the hot air blower turned on, the ventilation airflow above and below the OT is disrupted significantly. The rising thermal plumes from the hot air blower drag the squames above the OT and the side tables and then they are advected downwards toward the surgical site by the ventilation air from the ceiling. Temporal history of the number of squames reaching 4 imaginary boxes surrounding the side tables, the OT, and the patient's knee shows that several particles reach these boxes for the blower-on case.

KEYWORDS

forced air warming, large-eddy simulation, squames dispersion, ultra-clean ventilation

1 | INTRODUCTION

Microbial skin colonizers, such as *Staphylococcus aureus*, have been known as a major cause of surgical site infections (SSIs) in operating rooms.[1,2] These bacteria typically colonize on human skin cells or squames which are routinely shed by humans, roughly about 10^7 particles per day. The squame particle size is about 4 to 20 μm of equivalent diameter.[3,4] Reducing the bacterial colony-forming units (cfu) in surgical wounds is of great importance as it has been shown that it only requires about 10 cfu to cause a deep SSI after a joint replacement surgery.[5]

Reduction of post-operative SSIs caused by microbial skin colonizers has been linked to 2 main factors: (1) ultra-clean ventilation (UCV) systems and (2) perioperative patient warming.[2,5,6] Ultra-clean ventilation aims to reduce the quantity of airborne bacteria in the operating room (OR) and most importantly near the surgical site. This is typically achieved by the constant delivery of highly filtered ultra-clean air with a downward uniform velocity of 0.3 to 0.5 m/s.[7] The UCV

performance depends critically on volumetric airflow, proper temperature gradients, and use of uniform downward flowing ventilation air.[8,9] Medical equipment within OR and the medical staff can disrupt this airflow and create wakes, flow unsteadiness, and turbulence, thereby increasing the amount of bacterial cfu in the OR. It should, however, be noted that the effectiveness of UCV has not been fully proven clinically.[10] A systematic review and meta-analysis on UCV effectiveness was recently conducted by Bischoff et al.[11]

Perioperative patient warming is the other important clinical practice to prevent the core temperature of the patient dropping below 36°C and minimize the risk of hypothermia. Preventing inadvertent perioperative hypothermia has several benefits that include reduced operative blood loss and more importantly reduced transfusions, reduced wound infections, reduction in postoperative ulcers, reduction in morbid cardiac events, and reduced duration of hospital stay.[2,6] Forced air warming (FAW) devices have been used for over 2 decades due to their efficacy in maintaining patient's core body temperature. These devices use forced convection to increase the skin temperature and the total body thermal energy content. These devices use a blower (such as 3*M* Bair Hugger) that extracts the room temperature air through a high-quality fine-grained air-intake filter (typically 0.2 μm-rated), heats the air using a heating coil and vents the air into the sterile field adjacent to the operative site.[2,12,13] The filtered warm airflows through a connecting hose into a plastic blanket and exits the blanket through tiny holes over the patient's skin. A number of studies have examined the safety of forced-air warming, and whether FAWs can affect the SSIs through mobilized airborne contamination. Forced air warmings can potentially lead to surgical site contamination in 2 ways: (1) direct contamination of the air from the blower that reaches the patient's body and (2) disruption of the UCV air by the thermal plumes and turbulence. The former risk can potentially be reduced by using blower intake filters that are HEPA-rated and show high filtration efficiency. The latter has been studied extensively.[2]

It is hypothesized that the temperature gradients and resultant thermal plumes created by the FAW devices could disrupt the UCV flow that is designed to be uniform and downward and may lead to increased SSIs.[6,7,14-17] Temperature gradients and excess heating created by FAW devices can transport air from the floor level to the surgical site, thus increasing the potential risk of SSIs.[6,7,16,17] Moretti et al[14] measured an increase in the bacterial load when FAWs were used. Lack of flow visualization is the main drawback of these studies as they do not provide information about whether the particles came from the floor or from the FAW blower. Smoke particle visualization has been used[6,15] to understand the source of these particles near the surgical site comparing cases with no warming, FAW, and radiant warming. Although they found that FAW increased (by almost 10-fold increase) the particle count with blower turned on, they also showed that the uniform flow from the UCV reduced the effect of particles by limiting their numbers near the surgical site. The interaction between the UCV flow and the rising plumes from the forced-air warming devices plays a critical role in deciding whether FAWs indeed can lead to increased number of particles near the surgical site. However, there have not been detailed experimental measurements of flow patterns in the OR setting with the FAW blower turned on. Recently, particle-image velocimetry (PIV) measurements were conducted[18,19] to understand the flow pattern in an OR with the UCV system. This study, however, did not investigate the effect of FAW blower but made detailed measurements of temperature fields over the surfaces of mannequins representing a patient and medical staff for use in computational modeling. Although the above PIV was able to visualize and measure the flow field, it was limited to planar data (2D PIV) and thus a full three-dimensional data are not available for the OR. Nevertheless, some useful information on the flow unsteadiness, turbulence within the room was obtained.[19]

Computational fluid dynamics modeling is the only other way to characterize the turbulent flow field in an OR in detail to understand whether the hot air blowers can lead to increased dispersion of squames to the surgical site. Performing computational fluid dynamics accurately, however, is a difficult task due to the complexity of the turbulent airflow and the OR size including the medical equipment, staff, and lamps. Three basic approaches are available for predicting turbulent flows: (1) direct numerical simulation (DNS), (2) Reynolds-averaged Navier-Stokes (RANS) modeling, and (3) large-eddy simulation (LES). In DNS, the Navier-Stokes (NS) equations are solved on a computational grid that is fine enough, in space and time, to directly capture *all* the scales associated with the fluid flow motion without requiring any additional models.[20] This means that the computational grid in three-dimensions is small enough to capture the smallest scales of turbulence and the time-step is small enough to capture the smallest time-scale associated with the flow. DNS is prohibitively expensive and not practical for realistic engineering applications.

In RANS, the NS equations are averaged in time to obtain equations for the *time-averaged* velocity field. Thus, in this approach, only the mean velocity field that varies in space is calculated, and all information about the time-dependent fluctuations of the velocity field around the mean flow is lost. This time-averaging renders RANS computations the least expensive among the 3 available approaches. However, time-averaging the nonlinear inertial terms in the NS equations generates additional unknown terms that require closure models. Because these models and their empirical coefficients

are not universal, using them for a complex flow such as air circulation in an OR, invariably provides inaccurate results. Experimental data are necessary to adjust the empirical coefficients and thus the RANS models are not *predictive*. A majority of the numerical studies in the literature on OR airflow distribution and dispersion of squames are based on the RANS approach.[8,21,22] Since the instantaneous velocity field needed for calculating the trajectories of squames is not directly computed, the RANS model is incapable of accurately predicting the locations of squames at any time in the OR.

Memarzadeh and coworkers[8,21] investigated the effect of various UCV inlet flow conditions on the transport of squames in an OR. They considered a realistic OR geometry with medical staff, equipment, surgical lamps, etc, and accounted for the thermal plumes created by heat radiated from various sources but did not incorporate the FAW blower system together with a blanket covering the patient. They used a RANS model coupled with a Lagrangian particle-tracking of around 4000 representative particles. They showed that use of a uniform inlet flow with laminar conditions is better for reducing the number of particles near the surgical site. It is important to note that the literature uses the terminology "laminar flow" for the UCV flow. Based on the standard values of air changes per hour (ACH) for an OR (25 per hour), the air inlet flow Reynolds numbers are much larger than 2000, a critical value beyond which turbulence occurs in a duct. Although the level of turbulence in the inlet flow is not large (< 10%), the flow contains velocity fluctuations, and is unsteady and not laminar. In addition, they found that the thermal plume created by the hot surface of the surgical site prevented particles from reaching the site. They[8,21] showed that roughly 2% to 5% of particles reach the surgical site, *provided they are originated very close, about* 1.3 *cm above the site.* Particles originating from locations away from the surgery did not have a statistically significant probability of reaching the surgical site. Their study[8,21] provided some important insights into the OR airflow and motion of squames. If the objective is to accurately simulate the dispersion of inertial particles in a turbulent flow, then a three-dimensional, instantaneous velocity field is necessary to calculate the forces on the particles. Inertial particle trajectories and dispersion are strongly influenced by the spatiotemporal variations in the velocity fields of the carrier flow. Hence, using only the mean velocity field together with an ad hoc model for the velocity fluctuations, as is done in RANS,[8,21] provides inaccurate dispersion characteristics.[23,24] An improved RANS to capture the transient effects uses a model for particle motion that uses the local turbulence kinetic energy and introduces some randomness (typically a Gaussian distribution) in the particle equations[23] is necessary. However, predictions of particle dispersion using this improved RANS approach do not agree with the experimental data in a wide range of applications involving swirling, separated flows.[23,24]

Chow and Wang[22] investigated the UCV flow and its effect on bacteria-carrying particles in an OR using a RANS model as well. They simulated the bacteria particles as a non-inertial pollutant, wherein a Eulerian transport equation for the concentration of the bacteria is calculated. In addition, they considered periodic bending movement of one of the surgeons performing the operation. They found that if the surgical staff stands upright (no bending), the UCV flow keeps the bacteria concentration very low (< 1 cfu/m^3) near the surgical site. However, with the surgeon's bending motion included, they showed that this concentration increased to larger than the recommended value (10 cfu/m^3).

The published RANS studies[8,21,22] did not include the FAW blower system with a blanket covering the patient. To assess the interaction between UCV and FAW blower, an accurate predictive simulation is needed. Large-eddy simulation is a numerical method that involves computing the properties of the large, energy-containing eddies of turbulence accurately, without any user-adjustable coefficients, and models only the more homogeneous, small scales of turbulence.[20,25] In LES, the NS equations are spatially filtered (in contrast to time-averaging in RANS) using a local filter to obtain an instantaneous spatially filtered velocity field.[20] The filtering operation applied to the nonlinear NS equations creates additional unclosed terms that require modeling. However, in LES, modeling is applied only to the unresolved, subgrid scales (SGS), which are homogeneous and universal, and thus the SGS models produce accurate predictions for a wide range of turbulent flows. A dynamic procedure, typically used in LES-SGS modeling, renders the modeling process completely free of any user-defined tuning parameters in contrast to RANS. All SGS model coefficients are obtained directly in the calculations and are not set by the user. In LES, the resolved instantaneous velocity field at the particle location is used to compute the forces on the particles as opposed to the time-averaged velocity in RANS. Accordingly, the effect of the energetic turbulence scales (of the order of the grid resolution and larger) are completely captured in LES, thus predicting the particle dispersion directly. Particle dispersion predicted via LES[26-28] agrees very well with the experimental data, in contrast to RANS. Recent advances made in algorithmic developments for LES on arbitrary shaped unstructured grids[27,29] have facilitated application of LES to more realistic problems involving complex geometries and flow conditions. These advances have been successfully applied to turbulent, reacting flows in a gas-turbine combustion chamber and has led the gas-turbine industry to switch from RANS to the predictive LES technique in their design cycle.[27-29] At the time of writing this paper, only one LES study has been published for an OR[30] which investigated the flow of air into an isolation room during the opening and closing of a door and the passage of a human.

The main goal of the present study is to use LES to understand the interaction of the OR UCV airflow and the flow created by forced air warming system and investigate the effect of this interaction on the dispersion of squames. Specifically, computations are conducted for the cases with blower-off and blower-on, including the Lagrangian tracking of a large number of squames that are initially placed on the OR floor, to prove whether the FAW system plays a critical role in transporting the squames to the surgical site. As described below, in the present work, a high-fidelity, LES was performed to study the interaction of the OR UCV airflow with the flow created by a forced air warming system (3M Bair Hugger blower) and the effect of this interaction on the dispersion of squames. A full three-dimensional CAD of an OR with operating table (OT), surgical lamps, medical staff, side tables, a blower, and a patient undergoing knee surgery is used. However, additional complexities due to the movement of the medical staff reaching for the surgical instruments placed on the side tables are not included in the present study. It is anticipated that these complexities will further enhance the probability of dispersing the squames to the surgical site.

The rest of the paper is arranged as follows. Materials and methods are described in Section 2 that includes details of the OR geometry, the CAD model, and the numerical approach. This includes the OR dimensions, the surgical lamps, 4 medical staff, an OR table, 2 side tables, the blower, and the patient undergoing knee surgery. The numerical approach is described in Subsection 2.2. This includes a detailed discussion of LES, the governing equations, the computational grid, the boundary conditions, and the numerical algorithm. This is followed in Section 3 by detailed description of the results of the flow field, particle trajectories, and particle counts that reach the surgical site and other key regions of interest. Finally, the findings are summarized in Section 4.

2 | MATERIALS AND METHODS

This section describes the OR geometry and CAD model used for the OT, the surgeons, patient, side tables, the drape, and the blower system. This is followed by details of the numerical simulation including the numerical approach, the governing equations, computational grid, and numerical algorithm.

2.1 | OR geometry and CAD model

The OR CAD (computer aided design) model was created using Ansys SpaceClaim Direct Modeler (ANSYS, Inc, Canonsburg, Pennsylvania). The CAD model replicated a realistic OR depicting a knee surgery being performed on a patient. An original baseline CAD model was obtained from M/E Engineering P.C. and was further modified to incorporate the measured dimensions of the inlet air grilles and the surgical drape as shown below. Figure 1A shows the OR dimensions used to create the CAD model. The length, width, and height of the room are 7.32, 7.01, and 3.18 m, respectively. Figure 1B shows a closeup view of the surgeon's hands extended over the patient's knee mimicking a real-world operating procedure.

The CAD model also includes several items that are usually present in a real OR. These include (1) OR table, (2) OR drape, (3) patient's body under the drape with knee exposed, (4) four medical staff (2 have extended hands and 2 have hands down), (5) two side tables, (6) two surgical lamps, and (7) 3M Bair Hugger blower unit. The shape and dimensions of the drape near the front end are based on measurements taken in a real OR as shown in Figure 2B. For the CAD model (see Figure 2A), the front end of the drape was designed according to the dimensions A, D, C, and E in Figure 2A. The dimensions in the CAD model are given in both metric and imperial units (in brackets) in this figure to facilitate direct comparison with the picture on the right. The distance between the vertical bars holding the drape, denoted by dimension F in Figure 2B, was also implemented in the CAD model. The bottom of the OR table is 0.94 m above the floor of the room. The drape on the OR table covering the patient's torso is suspended such that its edge is 0.52 m above the floor.

The CAD model included 10 inlet grilles of same size (0.51 m × 1.12 m) for supplying clean, filtered air to the OR. There is a gap of 0.1 m between the neighboring grilles at all sides. There are 4 exhaust (or outlet) vents, 2 on each side wall. Each outlet grille is 0.71 m in width and 0.71 m in length.

2.2 | Numerical simulation

A state-of-the art, fully parallel, unstructured, colocated grid flow solver based on principles of kinetic energy conservation for LES[27] of turbulent flow in the limit of zero-Mach number is used in this study. This solver is MPI-based, uses algebraic multigrid for the pressure Poisson equation, and third-order WENO-based scheme for the transport of scalar fields such as temperature. It has been thoroughly validated for a number of different particle-laden turbulent flows[26,28] including swirling turbulent flow in a coaxial combustor, turbulent reacting flow, as well as spray combustion in a realistic Pratt and Whitney gas-turbine combustion chamber.[27,29]
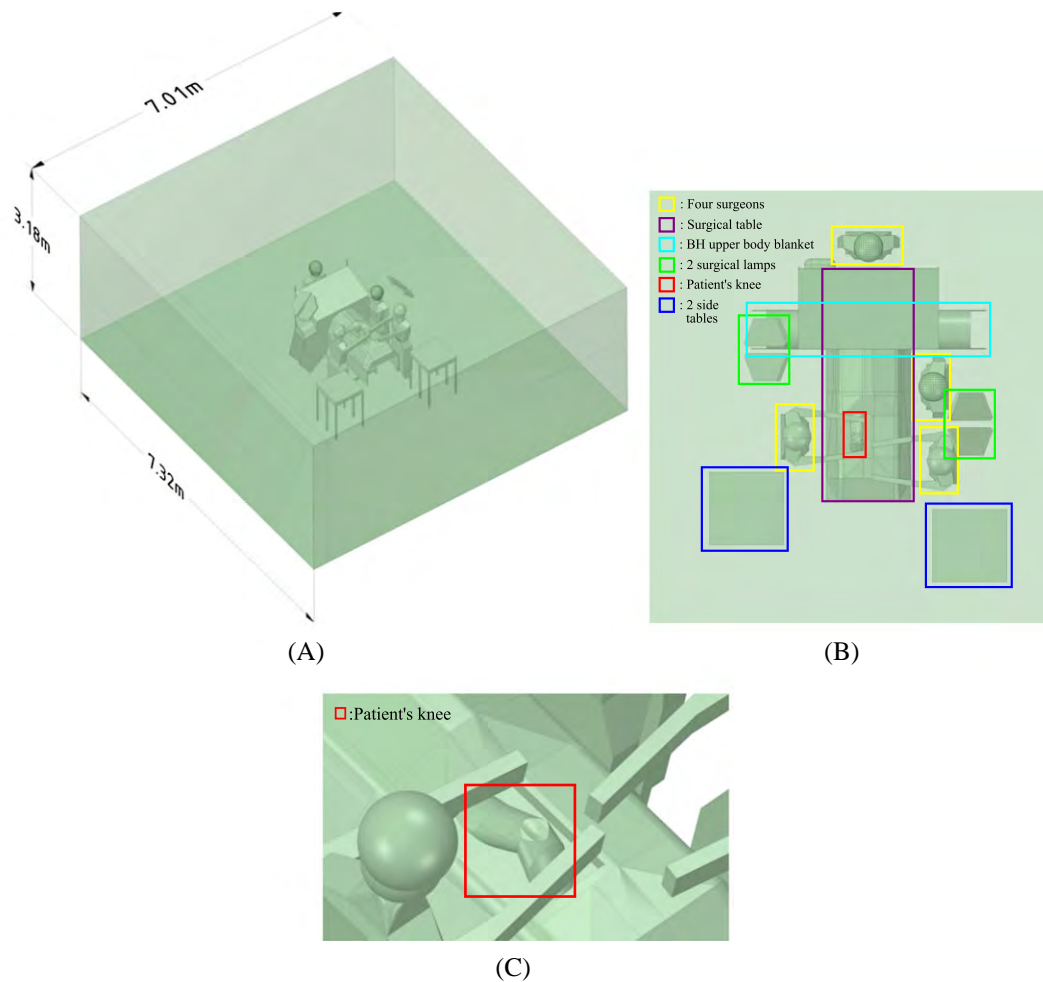
FIGURE 1 CAD model showing A, operating room dimensions, B, closeup view of various objects included in the CAD model, and C, close-up of the patient's knee
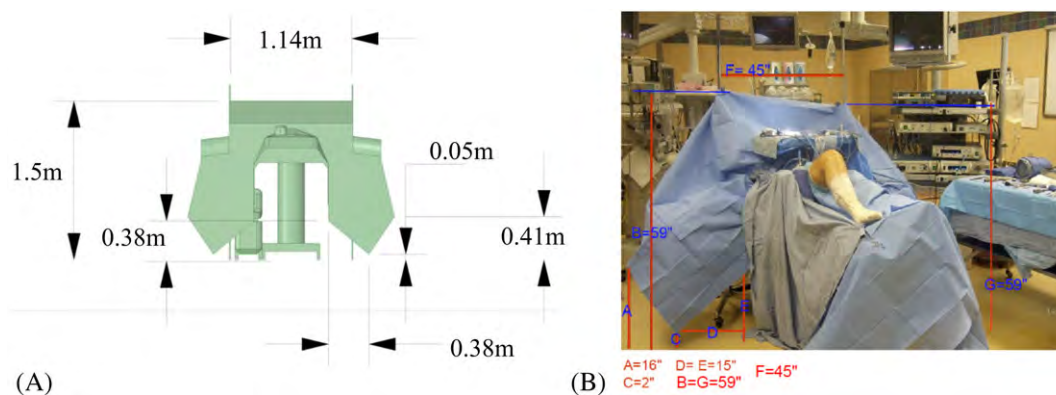

FIGURE 2 Drape dimensions and configuration: A, Model developed to match the drape dimensions. B, Actual drape picture in an operating room. The dimensions are shown in both metric and imperial units (in brackets)

2.2.1 | Governing equations

The airflow in an OR is subject to temperature variations owing to various thermal energy sources, such as the lamps, heat radiated from the medical personnel bodies, hot air discharged from a blower system, among others. The local temperature variations change the local air density. However, since the airflow in the room is at relatively low-speed (maximum velocity is about $u \sim 0.5$ m/s compared to speed of sound, $c \sim 343$ m/s), the Mach number (u/c) is small ($\ll 0.01$). Small Mach

number means that the convective time scales are much larger than acoustic time scales, and thus, the compressibility effects are negligibly small. Under these conditions, the variable-density equations in the limit of zero-Mach number are valid and used in the present study together with the ideal gas law, $\rho = P_0(R_{universal}/M_{air})T$, where $R_{universal}$ is the universal gas constant, M_{air} is the molecular mass of the air, T is the absolute temperature, and P_0 is the bulk thermodynamic pressure that is assumed constant at atmospheric pressure.

Gas-phase equations

The spatially filtered, Favre-averaged, governing equations used for LES of particle-laden, turbulent airflow with heat transfer and buoyancy effects are given as

$$\frac{\partial \overline{\rho_g}}{\partial t} + \frac{\partial \overline{\rho_g}\tilde{u}_j}{\partial x_j} = 0. \tag{1}$$

$$\frac{\partial \overline{\rho_g}\tilde{u}_i}{\partial t} + \frac{\partial \overline{\rho_g}\tilde{u}_i\tilde{u}_j}{\partial x_j} = -\frac{\partial \overline{p}}{\partial x_i} + \frac{\partial}{\partial x_j}\left(2\overline{\mu}\tilde{S}_{ij}\right) - \frac{\partial q^r_{ij}}{\partial x_j} + (\overline{\rho_g} - \rho_0)g_i, \tag{2}$$

$$\frac{\partial \overline{\rho_g}\tilde{h}}{\partial t} + \frac{\partial \overline{\rho_g}\tilde{h}\tilde{u}_j}{\partial x_j} = \frac{\partial}{\partial x_j}\left(\overline{\rho_g}\tilde{\alpha}_h\frac{\partial \tilde{h}}{\partial x_j}\right) - \frac{\partial q^r_{hj}}{\partial x_j}, \tag{3}$$

where

$$\tilde{S}_{ij} = \frac{1}{2}\left(\frac{\partial \tilde{u}_i}{\partial x_j} + \frac{\partial \tilde{u}_j}{\partial x_i}\right) - \frac{1}{3}\delta_{ij}\frac{\partial \tilde{u}_k}{\partial x_k}. \tag{4}$$

Here, $\overline{\rho_g}$ is the filtered density, $\tilde{u}_i$ is the Favre-averaged velocity field, $\overline{p}$ is the filtered pressure, μ is the dynamic viscosity, $\alpha_h = k/\overline{\rho_g}C_p$, is the thermal diffusivity (k is the conductivity and C_p the specific heat at constant pressure), g_i is the gravitational acceleration, and $\tilde{S}_{ij}$ is the filtered rate of strain. In addition, the specific enthalpy, $h = (T - T_0)/T_0$, where T is the local absolute temperature. Also, T_0 and ρ_0 are the absolute temperature and density fields corresponding to the air inlet conditions and pressure of P_0.

The additional terms q^r_{ij} and q^r_{hj} in the momentum and the enthalpy equations, respectively, represent the subgrid-scale stress and energy flux and are modeled using the dynamic Smagorinsky model.[31] The unclosed terms in Equations 2 to 3 are modeled using the gradient-diffusion hypothesis with eddy-viscosity/diffusivity,

$$q^r_{ij} = \overline{\rho_g}(\tilde{u}_i\tilde{u}_j - \widetilde{u_iu_j}) = 2\mu_t\tilde{S}_{ij} - \frac{1}{3}\overline{\rho_g}q^2\delta_{ij}, \tag{5}$$

$$q^r_{hj} = \overline{\rho_g}(\tilde{h}\tilde{u}_j - \widetilde{hu_j}) = \overline{\rho_g}\alpha_t\frac{\partial \tilde{h}}{\partial x_j}, \tag{6}$$

where the eddy viscosity (μ_t) and eddy thermal diffusivity α_t are calculated dynamically at each time-step and for each grid point using the dynamic procedure.[32] Details of the model may be obtained from Moin and Apte.[27]

Equations for calculating the trajectories of individual squames

The typical human skin cells or squames are disc-shaped with a diameter ranging from 4 to 20 μm and a thickness of 3 to 5 μm with density close to that of liquid water (1000 kg/m^3).[3,33] Although the squames shape is more disc-like, they are considered in the present study as nondeformable, spherical in shape. A spherical shape is assumed as the dynamics of the spherical particle is easier to calculate and also the lift and drag forces on small particles of disc or spherical shape are not significantly different. The diameter of the spherical particle is calculated to be 10 microns to have its average settling velocity equal to that of a disc-shaped particle moving either normal or parallel to the mean flow. Recent studies using RANS[8,21] also approximate the squames as spheres of diameter 10 microns.

A Eulerian-Lagrangian approach is used wherein individual squames trajectories are tracked in a Lagrangian frame. The different forces on the particles is calculated using standard laws. The effect of the particles on the fluid flow is negligible owing to their small concentration and thus a one-way coupling approach is adopted, wherein the squame motion uses the fluid velocity to compute the forces, but the effect of squames on the fluid momentum is neglected.[34] In addition, since the volume fraction of the squames in an OR is small ($\ll 10^{-3}$), collisions among the squames are neglected. The squame particle motion equation is that of Maxey and Riley,[35]

$$\frac{d}{dt}(\mathbf{x}_p) = \mathbf{u}_p, \tag{7}$$

$$m_p\frac{d}{dt}(\mathbf{u}_p) = \mathbf{F}_g + \mathbf{F}_d + \mathbf{F}_\ell, \tag{8}$$

where $\mathbf{x}_p$ is the particle (squame) centroid location, m_p is the mass of an individual particle, $\mathbf{u}_p$ is the particle velocity, $\mathbf{F}_g$ is the gravitational force, $\mathbf{F}_d$ is the drag force, and $\mathbf{F}_\ell$ is the lift force.

The large ratio of particle density to air density, ρ_p/ρ_g, renders both the Basset history force and the added mass force negligible compared to the drag force. The ratio of the Saffman lift to the drag force is given by, $F_\ell/F_{drag} \sim \rho_g d_p^2 (du/dy)^{1/2}/\mu$, and is dependent on the shear rate and particle diameter. For particles with small diameter and low inertia, this force can also be neglected in comparison to the drag force.[36,37] The lift force is incorporated in our calculations to account for the saltation of the squame particles from the OR floor. The gravity, drag, and lift forces are given as

$$\mathbf{F}_g = (\rho_p - \bar{\rho}_g)\mathcal{V}_p\mathbf{g}; \quad \mathbf{g} = -9.81 m/s^2, \tag{9}$$

$$\mathbf{F}_d = -\frac{1}{8}C_d\bar{\rho}_g\pi d_p^2|\mathbf{u}_p - \tilde{\mathbf{u}}_{g,p}|(\mathbf{u}_p - \mathbf{u}_{g,p}); \quad C_d = \frac{24}{Re_p}(1 + 0.15Re_p^{0.687}), \tag{10}$$

$$\mathbf{F}_\ell = -C_\ell m_p\frac{\bar{\rho}_g}{\rho_p}(\mathbf{u}_p - \tilde{\mathbf{u}}_{g,p})\times(\nabla\times\tilde{\mathbf{u}}_g)_p; \quad C_\ell = \frac{1.61\times6}{\pi d_p}\sqrt{\frac{\mu}{\rho_g}|(\nabla\times\tilde{\mathbf{u}}_g)_p|}, \tag{11}$$

where the subscript p represents the squame particle, $\tilde{\mathbf{u}}_{g,p}$ represents the fluid velocity interpolated at the particle center location, $\mathcal{V}_p$ is the particle volume, d_p is the particle diameter, $Re_p = \bar{\rho}_g|\mathbf{u}_p - \tilde{\mathbf{u}}_{g,p}|d_p/\mu$ is the particle Reynolds number, C_d is the drag coefficient, and C_ℓ is the lift coefficient. The fluid velocity, $\tilde{\mathbf{u}}_{g,p}$, in the particle equations above, is computed at individual particle locations within a control volume using a generalized, trilinear interpolation scheme for arbitrary-shaped elements.

After obtaining the new particle positions, the particles are relocated, particles that cross interprocessor boundaries are duly transferred, boundary conditions on particles crossing boundaries are applied, source terms in the gas-phase equation are computed, and the computation is further advanced. Solving these Lagrangian equations thus requires addressing the following key issues: (1) efficient search and location of particles on an unstructured grid, (2) interpolation of gas-phase properties to the particle location for arbitrarily shaped control volumes, and (3) inter-processor particle transfer. The details of the Lagrangian particle tracking algorithm on unstructured grids are provided by Apte et al.[26,28] In addition, if the squames impact internal boundaries, a simple, perfectly elastic specular reflection is assumed wherein the squames reverse the wall-normal velocity and preserve the wall-tangential velocity. If the squames impact the patient's knee or the inlet (suction port) of the 3M Bair Hugger blower system, they are assumed to stick to the surface and are no longer advanced in the computations.

Numerical scheme

The computational approach is based on a colocated, finite-volume, energy-conserving numerical scheme on unstructured grids[27,29] and solves the variable density fluid flow equations in the limit of zero-Mach number. In this colocated scheme, the velocity and pressure fields are stored and solved at the centroids of the control volumes. Numerical solution of the governing equations of the fluid phase and particles (squames) are staggered in time to maintain time-centered, second-order advection of the fluid equations. The scalar field (enthalpy or nondimensional temperature; Equation 3 is advanced using the old time-level velocity field. A second-order WENO scheme is used for scalar advective terms and centered differencing for the diffusive terms. All terms, except the source term due to buoyancy, are treated implicitly using Crank-Nicholson for temporal discretization. Details of the numerical algorithm are given in Appendix A.2. Once the scalar field is computed, the density and temperature fields are obtained from constitutive relations and the ideal gas law. The steps involved in solving the projection-correction approach for the velocity field together with validation studies for complex flow configurations are described in detail in Mahesh et al.[26-29] The squames equations are advanced using a fourth-order Runge-Kutta scheme.[26,28] The details of the Lagrangian particle tracking algorithm on unstructured grids is well documented by Apte et al.[26,28] If the squames impact internal boundaries, a simple, perfectly elastic specular reflection is assumed. If the squames impact the patient's knee or the inlet (suction port) of the 3M Bair Hugger blower system, they are assumed to stick to the surface and are no longer advanced in the computations.

Validating any numerical simulation of a three-dimensional turbulent flow in a complex geometry (such as the OR with all its contents including the Bair Hugger) is a prerequisite for trusting the results. The best way to validate the results is to compare them with high-quality experimental data for the same flow. High-quality experimental data for the three-dimensional velocity field of this flow require PIV. No such data exist in the literature due to large commensurate cost. In the absence of such data, the next best way to validate the computer code is to compare its results with high-quality experimental data for flows containing most of the important physical phenomena that exist in the OR flow, namely, turbulence, fluid density variation due to heating by different sources, external acceleration field such as gravity or swirl, and dispersed particles.

The LES solver has been thoroughly verified and validated with published results in refereed journals over the past 15 years. The LES solver has been applied to a range of incompressible and low-Mach number flow problems with and

without chemical reactions as well as with and without dispersed inertial particles. The flow solver has been verified and validated for the following cases:

1. Taylor-Green vortex on structured as well as unstructured grids. To show the robustness and good predictive capability of the numerical solver on unstructured grids, a standard test case of decaying Taylor Green vortices was simulated and compared with analytical solutions.[38]
2. Isotropic turbulence, turbulent flow in a channel, flow over a circular cylinder.[38,39]
3. Swirling, turbulent flow in a coaxial chamber giving rise to recirculation regions and swirling jets on unstructured grids.[26,29]
4. Turbulent reacting flow in a coaxial combustion chamber involving gas-phase chemical reactions modeled using the flamelet approach.[27,29,40] This demonstrates the accuracy of the solver in capturing scalar fields such as (mass fractions, temperature, etc) using the low-Mach number formulation.
5. Particle-laden, turbulent swirling flows in a coaxial chamber on unstructured grids. This validates the accuracy of the numerical solver in capturing inertial particle dispersion in complex flows and using unstructured grids.[26,28,41-45] Here, inertial particles include solid particles, bubbles (for cavitation studies), and droplets (for sprays and spray combustors).
6. Swirling, turbulent flow without combustion through a gas-turbine injector and a combustion chamber involving various complex flow patterns and using hybrid mesh elements such as hexes, pyramids, terahedrons, and wedges similar to those used in the present study.[27-29,40] To truly test the predictive capability of the solver, a blind prediction of the flow field was made which involved using only the CAD file for the flow configuration and properly defined boundary conditions. A prediction was made based on this information for flow velocity at different planes from the injector. The predicted velocity profiles were then compared with the experimental data to evaluate the accuracy of the solver.
7. Reacting flow in a realistic Pratt and Whitney combustion chamber with the physics of droplet breakup and evaporation[27,29] showing good agreement with the experimental data.

Many of the above studies include complex flows with mixing, local temperature gradients, and inertial particles in complex configurations. These extensive validation studies thus show that the code is versatile, accurate, and is capable of handling multiphysics, turbulent flow problems in a wide range of applications.

2.2.2 | Computational grid

A computational mesh was generated using both tetrahedral and hexahedral cells. The transition of mesh from tetrahedral cells to hexahedral cells was done using a combination of pyramid and wedge-type cells. Care was taken to generate a computational grid that minimizes the grid skewness as much as possible. In the regions away from the complex OR configuration involving the surgeons, the tables, the patient, and the drape, a mostly hex-dominant mesh is used. Closer to the OT, the computational grid is transitioned to a predominantly tetrahedra-based mesh. Details on the grid in the inlet region, surrounding the table and surgeon, are given in Appendix A.1. The total mesh count for the computational domain is about 66 million. Near the air inlet cross-sections, the grid is appropriately refined to capture the shear layer generated by the inlet flow between the grilles. The mesh surrounding the OR table, patient, surgeons, side tables, the blower, and surgical lamps is predominantly tetrahedral. The tetrahedral mesh was carefully refined to capture surface curvature. Extra refinement was performed near the surfaces in close proximity to other surfaces. This enhanced mesh refinement ensures that the effect of surface shapes on the flow and particle trajectories going around them is captured by the simulation. Overall, a high-quality mesh was generated for the present LES investigation. The minimum tetrahedral cell size (defined as the cube root of the cell volume) used near all key regions such as drape, patient, operating bed, and surgeons is about 1mm. The smallest grid spacing resolving the gaps between closely placed surfaces is 0.7mm. The coarsest tetrahedral cell size used away from the key regions is 2.5 cm.

A uniform hexahedral cell size of 1.5 cm is used to resolve the air inlet grille faces with 20 cells along its width and 44 cells along its length. The gaps between the inlet grilles are resolved using a finer mesh with each cell size of 0.63 cm. To capture the inlet airflow structures properly, a refined uniform mesh of 0.33cm is used along the flow direction. Finally, a uniform cell size of 2.5 cm is used to resolve each outlet grille with 28 cells along its width and 28 cells along its length. Various mesh metrics were checked to ensure that the quality of the generated mesh was good; details of which are given in Appendix A.1. The average skewness was 0.14 and the maximum skewness was 0.91. Only 0.018% of cells had total skewness greater than 0.8 indicating the high quality of cells in the mesh. Another mesh metric that was checked was the

aspect ratio of cells. The maximum aspect ratio was 16.2 and the average cell aspect ratio was 2.9, which indicate that a majority of cells in the mesh were of acceptable aspect ratio.

To capture the fluid flow near the bottom and predict the lift-off and dispersion of squames, a wall-normal grid resolution of 2.1 (in wall units) is in a region covering the floor under the OT and the surgeons. The wall-normal resolution is coarsened to about 5 (in wall units) further away from this region of interest. Finally, to resolve the wake regions and flow separation from the top surfaces of the medical staff, the grid is stretched and refined as shown in Appendix A.1.
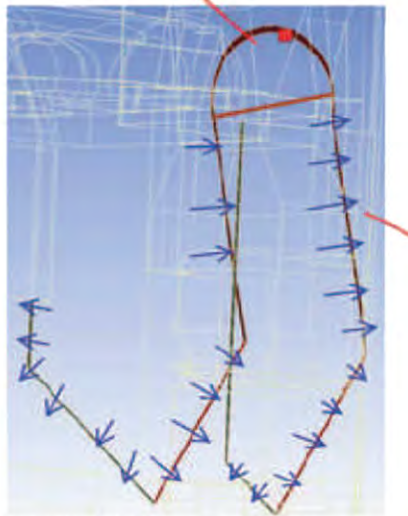
2.2.3 | Boundary conditions

Table 1 provides details of all boundary conditions used in the calculation, starting with OR air inlet conditions, heat transfer sources, BH hot air blower inflow (suction) and outflow, and OR air outlet conditions. There are 10 inlet grilles supplying air. The net supply air volumetric flow rate, $\dot{V}$, is 1.10436 m^3/s(0.39 ft^3/s). Using the inlet flow rates, the number of air changes per hour (ACH) of the OR is 24.45, which is the recommended value according to the ASHRAE handbook.[8] The inlet boundary conditions are imposed at the 10 grilles on the ceiling of the OR to model the inlet part of the forced ventilation system. Using the inlet flow rates, the number of ACH of the OR is 24.45., which is the recommended value according to the ASHRAE handbook.[8] The average inlet velocity, $\overline{U}_{in}$, is 0.1933m/s based on, $\overline{U}_{in} = \dot{V}/(10 \times A_{grill})$, where A_{grill} is the area of the cross-section ($1.12 \times 0.51 = 0.5712$ m^2) and $\dot{V} = 1.1044$ m^3/s(39 ft^3/s) is the net inlet volumetric flow rate. The air temperature of the inlet flow, T_{in}, is set to 59°F(15°C). Based on Reynolds number for the inlet grilles, $Re_{in} = 9226.54$ (Table 1), the inlet flow is turbulent. To have a completely predictive numerical simulation and to minimize the effect of boundary conditions, it is necessary to impose a proper, fully developed turbulent flow field at the inlet. Thus, a periodic turbulent duct flow was computed to produce a target mean flow rate equal to that prescribed using a body force technique.[46] This also generates turbulence fluctuations at the inlet plane that satisfy the continuity equation. The cross-sectional area of the periodic duct used is the same as that of each grille (1.12 m $\times 0.51$ m), and the length is about 4.5 times the hydraulic diameter of the cross-section. The velocity field data at the inlet cross-section was recorded in time series for almost 400 seconds of physical time. The turbulence intensity ($I = \sqrt{\frac{1}{3}(u_{rms}^2 + v_{rms}^2 + w_{rms}^2)}/\overline{U}_{in}$) at the inlet cross-section is 5% to 6% of the mean inlet velocity ($\bar{U}_{in}$) and is in agreement with the experimental measurements.[18,19] Here, u_{rms}, v_{rms}, and w_{rms} are the root mean square velocity components in the x, y, and z directions, respectively.

A 3M Bair Hugger 750 upper body blower draws air from the floor of the OR, heats it and discharges it into the blanket that covers the torso of the patient. The blanket is covered with a plastic drape. The maximum flow rate of the blower is

TABLE 1 Operating room characteristics

Parameter	Value
Room dimensions [m], L, W, H	$7.315 \times 7.00 \times 3.175$
Supply airflow rate [m^3/s], $\dot{V}$	1.10436
ACH [1/hr]	24.45
Room air temperature [°C]	15
Inler air density [kg/m^3], ρ_{in}	1.225
Supply air temperature [°C]	15
Room air pressure [Pa]	1.0131×10^5
Grille dimensions [m]	1.12×0.51
Grille Area [m^2]	0.5712
Grille hydraulic diameter [m], D_h	0.7
Mean inlet velocity [m/s], $\overline{U}_{in}$	0.1933
Inlet Reynolds number, $Re_{in} = \frac{\rho_{in}\overline{U}_{in}D_h}{\mu}$	9226.54
Inlet volume flow rate $\dot{V}$, [m^3/s]	1.1044
Temperature of inlet grille air, [°C]	15
Mean inlet velocity [m/s], $\overline{U}_{in}$	0.1933
BH blower volume flow rate $\dot{V}_{blower}$, [m^3/s]	0.021
Temperature of hot air injected along drape, [°C]	41.11
Heads of the surgeons and patient, [°C]	31.44
The patient's knee, [°C]	37.78
Two surgical lamps, [°C]	34.4

FIGURE 3 Heated blower air entering the operating room along the drape edge

$\dot{V}_{\text{blower}} = 0.021 \text{ m}^3/\text{s}$. The hot air leaves the blanket through 1000 (1 mm diameter) holes facing the patient and moves along the surface of the drape that covers the blanket and then is discharged into the room along the drape edges. In the present calculation, the bottom surface (facing the floor) of the blower is considered as a suction surface with surface area ($A_{extraction} = 0.03796 \text{ m}^2$). A Dirichlet boundary condition is applied at the suction surface of the blower that prescribes the extraction velocity $\overline{U}_{extraction} = \dot{V}_{blower}/A_{extraction}$, giving an extraction velocity of 0.5532 m/s. A Dirichlet boundary condition is applied along the drape edge such that the heated air enters into the room perpendicular to the edges of the drape with velocity, $\overline{U}_{drape} = \dot{V}_{blower}/A_{drape} = 0.2694$ m/s, where $A_{drape} = 0.07794 \text{ m}^2$ is the drape area. Figure 3 shows one portion of the drape edge and the heated air entering the OR from its edges. The temperature of the hot air leaving the drape edge is set equal to $106°F$ ($41.11°C$). Table 1 summarizes the temperature conditions specified for different surfaces in the CAD model. Other heat transfer sources in the OR are mainly the medical staff, patient, surgical lamps, and exposed surface of the patient's knee and a Dirichlet condition was used for the temperature at these surfaces based on the experimentally measured values.[18] All other solid surfaces were assumed adiabatic.

3 | RESULTS

The numerical simulation was initiated with stagnant air (zero velocity) in the OR and proper boundary conditions. All calculations were performed on a parallel computer and used 1600 processors. A simulation was conducted with the blower-off for about 121 seconds, which corresponds to about 8 flow through times based on the average inlet air velocity and the height of the room. This established a stationary flow with the thermal plumes created by the surfaces with higher-than-ambient temperatures. With the blower-off, the time-step used in the calculation was $\Delta t = 6 \times 10^{-5} s$ giving a CFL number of about 0.75. This time step was sufficient to resolve the important time scales of turbulence and particle motion accurately. The flow statistics were collected for a total of 80 seconds after a stationary flow field was established. The turbulence statistics were collected over the entire three-dimensional region and data were sampled at each time-step. Although full three-dimensional data are available, only certain slices in the domain of interest are shown in the present work. Three million squame particles were placed at the floor in 3 different regions surrounding the OT as described below and the squames trajectories were calculated for about 21 seconds.

After the above calculation with blower turned off was completed, the remaining squames in the computational domain were removed, and the blower was turned on. With the blower discharging a hot air at higher speeds, the time-step was

reduced by a factor of 2.5 to $\Delta t = 2.4 \times 10^{-5}s$ maintaining the CFL number about 0.6. The reduction in time step is related to both the explicit treatment of the gravitational source term in the momentum equation as well as increased velocity at the blower discharge location. A calculation was performed for about 30 seconds to obtain a developed plume from the hot air discharged by the blower. Calculation of the flow statistics was then activated and initial locations of 3 million squames were prescribed. With the blower-on, the flow statistics were collected for about 37 seconds and particle trajectories were calculated for about 30 seconds.

All calculations were performed on a parallel computer and used 1600 processors. The computational domain was decomposed such that each processor contains roughly the same number of control volumes. The overall calculation (including initial transient, the case with blower-off, and the case with blower-on including particle trajectories for both cases) took about 2M CPU-hours. For the case of blower-off, about 20 seconds of physical time would cost roughly 100 000 CPU-hours, whereas the same calculation with blower-on would cost roughly 220 000 CPU-hours. For each case, tracking
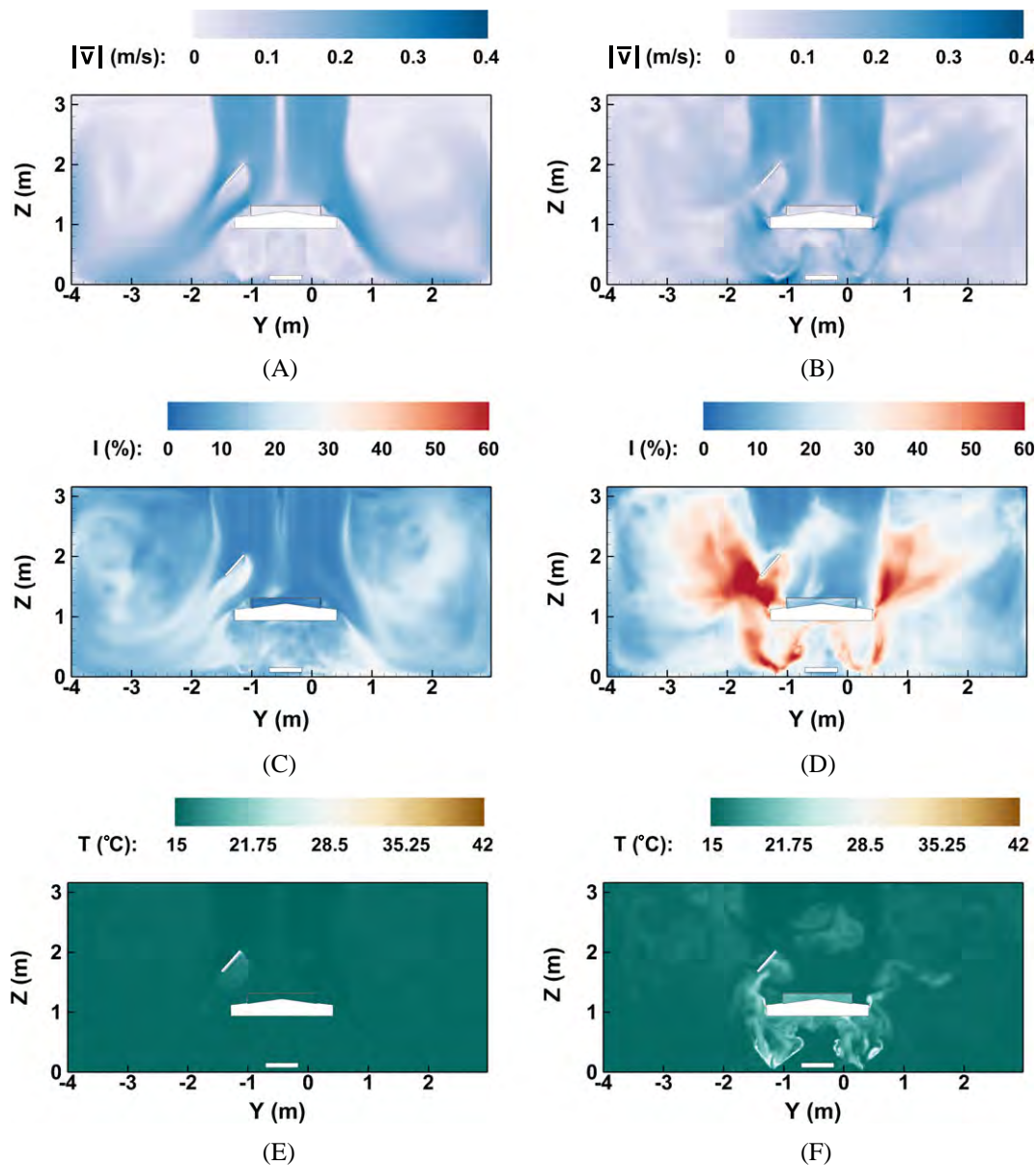

FIGURE 4 Contours of the mean velocity magnitude and the turbulence intensity at $x = -0.88m$. A, Mean velocity with blower-off. B, Mean velocity with blower-on. C, Turbulence intensity with blower-off. D, Turbulence intensity with blower-on. E, Instantaneous temperature with blower-off. F, Instantaneous temperature with blower-on. The time average is taken over a physical time of $80s$ (no blower) and $37s$ (with blower) after establishing a stationary state. The temperature snapshots are at about $35s$ after a stationary flow field is established

3 million trajectories of squames increased the computational cost by about 20% to 30%. This is because, initially, the squames are clustered in a small region near the floor causing load imbalance as the particles were present on only a few processors. The flow statistics and particle trajectories are discussed below.

3.1 | Flow characteristics

Figure 4A-D shows the contours of mean velocity magnitude and turbulence intensity for the 2 cases of blower-off and blower-on in a planar slice of the OR at $x = -0.88$ m. The slice includes the surgical lamp and the OT. For the case of blower-off, Figure 4A shows that the ventilation air from the ceiling inlet grilles moves downwards, gets deflected by the surgical lights and the table, impinges on the floor farther away from the table, and finally exits through the outlet grilles. Large recirculation regions are created on both sides of the OT. In comparison, with the blower turned on, the flow underneath and around the OT is considerably modified as can be seen from the large velocity magnitudes under
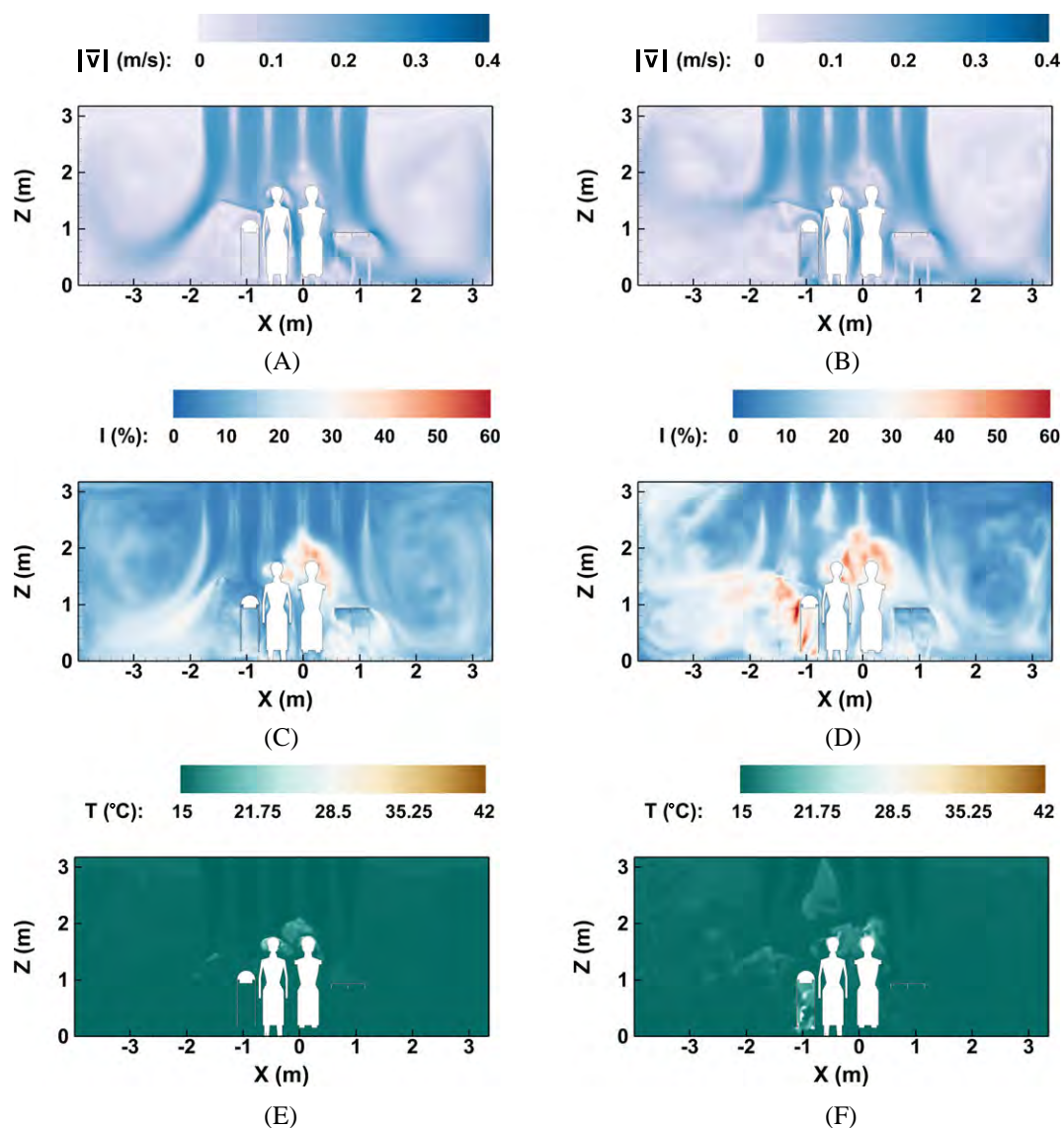

FIGURE 5 Contours of the mean velocity magnitude and the turbulence intensity at $y = -0.162m$. A, Mean velocity with blower-off. B, Mean velocity with blower-on. C, Turbulence intensity with blower-off. D, Turbulence intensity with blower-on. E, Instantaneous temperature with blower-off. F, Instantaneous temperature with blower-on. The time average is taken over a physical time of $80s$ (no blower) and $37s$ (with blower) after establishing a stationary state. The temperature snapshots are at about $35s$ after a stationary flow field is established

the OT (Figure 4B). The recirculation region is also disrupted by the rising air from the hot blower discharge. This difference is clearly visible by comparing the turbulence intensity contours shown in Figure 4C,D. With the blower-off, the maximum turbulence intensity level is about 30% in the high shear regions between the inlet air streams, as well as near the warm surgical lights due to the buoyant plume. With the blower-on, the turbulence intensity level increases to 60% in regions affected by the rising thermal plumes from the blower hot air. The instantaneous temperature contours shown in Figure 4E,F confirm that the increased turbulence level is mainly because of the thermal plumes from the hot blower air as can be seen by the high temperature regions under the OT.

Similarly, Figure 5A-D shows the contours of mean velocity magnitude and turbulence intensity for the 2 cases of blower-off and blower-on in a planar slice of the OR at $y = -0.162$ m and Figure 5E,F show the corresponding temperature contours. Similar trends as described before are observed. The hot blower air and the rising thermal plumes disrupt the downward ventilation airflow. The high temperatures and turbulence intensity under the inverted U-shaped drape are clearly visible. The flow is also highly asymmetric with the blower turned on owing to the orientation and location of the drape. It is also seen from Figure 5F that the rising thermal plumes may reach the ceiling in some regions. With the blower off, however, the plumes from warm surfaces of surgical lights, surgeons heads, and patient's knee are weak and are not significant enough to disrupt the downward ventilation airflow.

3.2 | Dispersion of squames

Three million particles with a diameter of 10 μm are initially placed within a U-shaped region of 1cm thickness above the floor of the OR, providing a least probable scenario for the squames to be carried to the surgical site by the air convection. This region is located around the OT, surrounding the feet of 4 surgeons present in the CAD model. To better visualize the trajectories of the squames originating from different initial locations, the U-shaped region is divided into 3 rectangular sections color-coded as (1) red, (2) green, and (3) yellow as shown in Figure 6. One million squames are placed in each of the three sections at the same time, providing equal probability for the statistical analysis of motion of squames. The position of an individual squame particle in a section is chosen randomly using a uniform distribution. If these squames are lifted by the turbulent air and moved to the surgical site, then other excluded actions such as the motion of medical equipment and staff and shedding of additional squames from the heads and faces of medical staff and surgical garments would increase the probability of the squames reaching the surgical site.

To visualize the effect of the hot blower air on the trajectory of squames, instantaneous scatter plots of squames are displayed at 20 seconds after their initiation with blower-off and blower-on in Figure 7A,B, respectively. Figure 8A-D shows close-up for 2 different views at the same instant. Drastic differences between the blower-off and blower-on cases are observed. It is clear from these figures that when the blower is off, the majority of the squames are dispersed by the ventilation airflow towards the outlet grilles. None of the squames actually rise to the level of the side tables or the OT. In contrast, in the case of blower-on, a large number of squames are lifted upwards by the rising thermal plumes. Some of
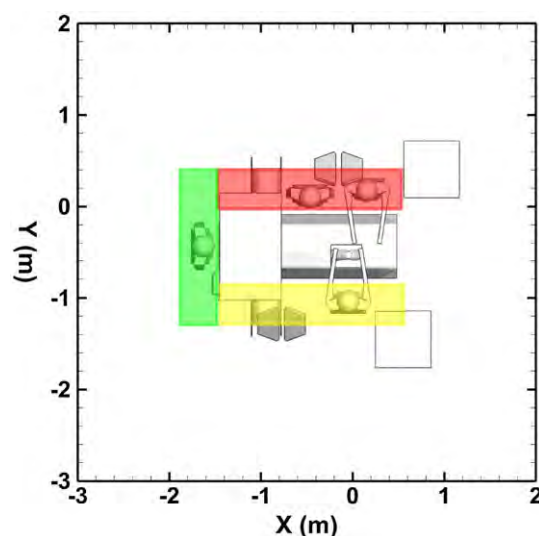

FIGURE 6 Three color-coded regions where the 3 million squames were initially distributed within a 1cm height from the floor
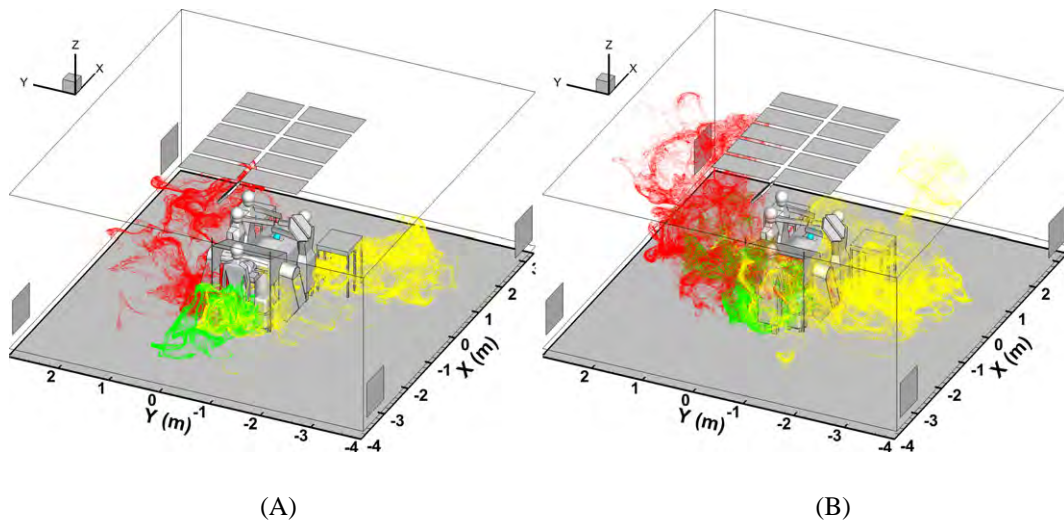
(A)   (B)

FIGURE 7   Instantaneous scatter plot of squames color-coded by their region of origin at 20 s after initiation: A, Blower-off. B, Blower-on

(A)   (B)

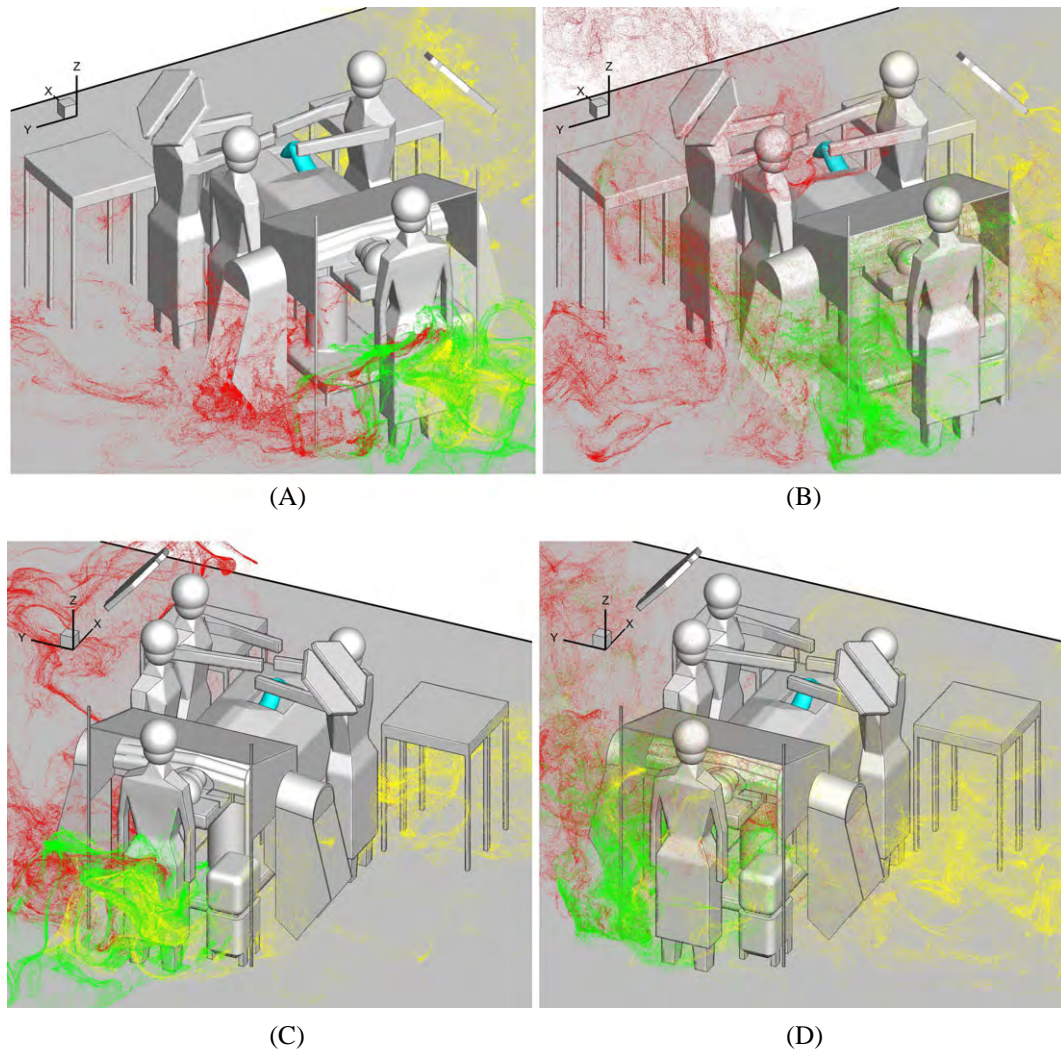(C)   (D)

FIGURE 8   Zoom-in views of the instantaneous scatter plot of squames color-coded by their region of origin at 20 s after initiation. A,C, Blower-off. B,D, Blower-on. Top and bottom rows represent 2 different views of the same plot

the squames (mostly red-colored and some yellow-colored) are lifted above the surgeons heads and are advected towards the OT by the incoming ventilation air. Large number of squames are seen to be above the OT, several are surrounding the surgeons hands, above the side tables, and some are very close to the patient's knee and the surgical site.

To assess the probability of the squames reaching the surgical site, 4 imaginary boxes were positioned as follows: 2 boxes covering the 2 side tables, a box around the OT, and a box around the patient's knee area. It is expected in an OR that the medical staff use surgical instruments placed on the side tables. The possibility of squames reaching the surgical site is then dependent on the number density of squames within these 4 imaginary boxes (see Figure 9). The number of squame particles inside the 4 boxes are recorded in time. A blue box (Figure 9A,C) is covering the whole OT. The height of the box is 30cm, and it surrounds the patient's whole body and the surgeon's hands. An orange box (Figure 9B,D) is placed above the OT, just covering the patient's knee and part of the surgeon's hands, and the top of the box is only 2 cm above the surgeon's hands. One purple box (Figure 9A-D) is placed on each of the 2 side tables. The height of these boxes is about 1 cm, so that any surgical instrument placed on the side tables would be within the box.

Two computations of the trajectories of squames were performed after a statistically stationary flow field has been reached for the cases of blower-off and blower-on. Based on the average inlet air velocity and the height of the OR ceiling, it takes 15 to 20 seconds for a fluid particle to travel from the air inlet grille to the floor. For the case of blower-off, only the ventilation air and thermal plumes created by the warm surfaces including surgical lights, surgeons' heads, patient's head, and patient's knee are responsible for the dispersion of squames. It was found that all the squames initiated in all 3 sections (red, green, and yellow) are basically transported by the airflow reaching the floor and quickly advected to the 4 outlet grilles. After the computation advanced to about 25 seconds of physical time, some squame particles do rise to the underside of the side tables, but none of the squames was found to enter the 4 imaginary boxes representing the regions of interest. It was concluded that without the hot air discharged from the blower, the ventilation air circulation alone
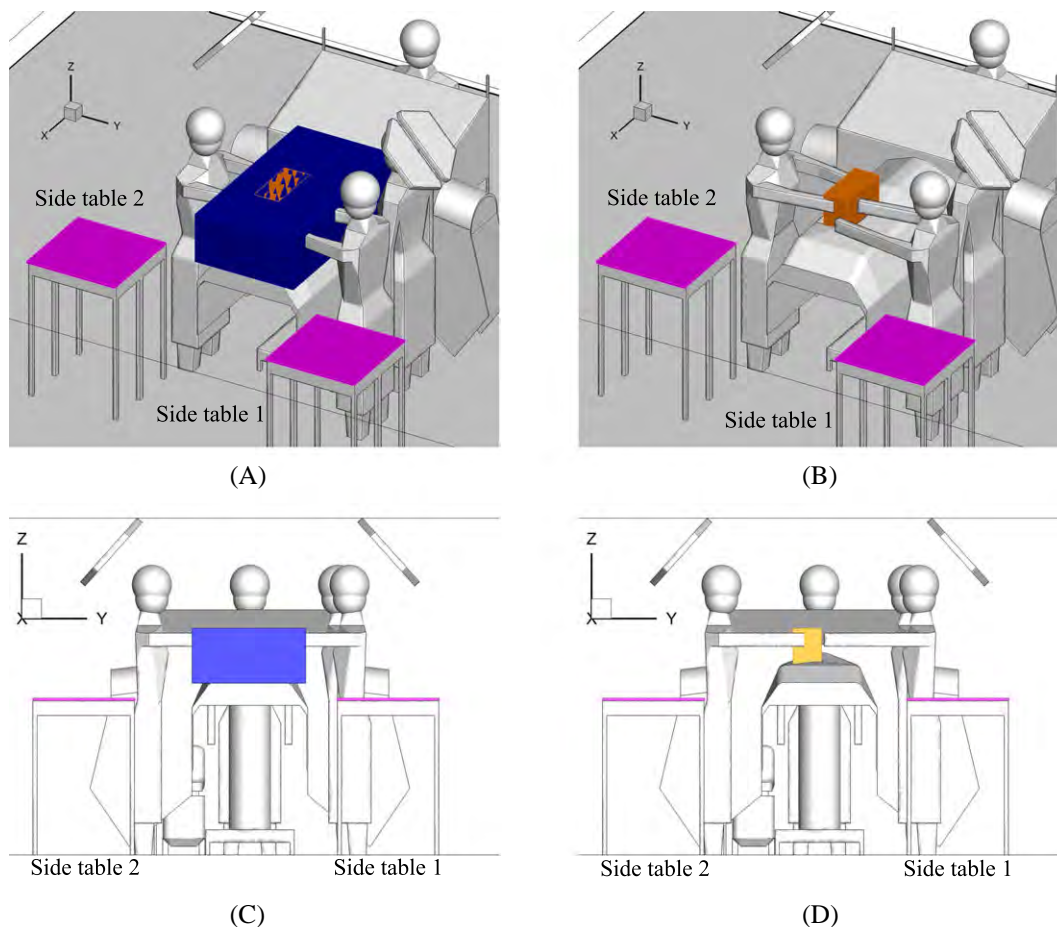

FIGURE 9 A-D, Four color-coded regions of interest, for recording the temporal history of the number of squames reaching them, shown in different views. The regions of interest include the zones above the 2 side tables, above the operating table, and above the patient's knee

cannot disperse the squames to the surgical site. The thermal plumes from various warm surfaces only slightly affect the air coming from the inlet grilles and do not affect the motion of the squames.

With the blower turned on, hot air is discharged along the drape sides that cover the patient's arms into the ambient air and strong thermal plumes rise under the OT. Some edges of the drape are very close to the floor (see Figure 2B) and the hot air plume drags the squames upwards faster than in the case when the blower was off. A majority of the squame particles are advected away from the OT towards the outlet grilles. However, a statistically significant number of particles are lifted above the OT with some reaching the height of the surgeons. The particles rise due to buoyancy and then get flushed down onto the OT by the incoming ventilation air from the inlet grilles. The particles then do enter the imaginary boxes of interest, specifically the boxes above the OT and the patient's knee.

Figure 10A-D shows the number of squame particles as a function of time entering the 4 imaginary boxes of interest (above the side tables, above the OT, and patient's knee). It can be seen that no particles are found inside the 4 boxes during the first 17 seconds, which is about the time needed for the ventilation air to travel from the ceiling to the floor. After this time, the number of squame particles in the box above the OT (Figure 10D) increases almost in a linear fashion. Within 30 seconds of physical time, the number of squame particles within the OT box are about 2500 and increasing. Figure 10C shows that at about 23 seconds, some of the particles above the OT start to enter the box above the knee, which is a very narrow zone surrounding the patient's knee. The number of these particles increases linearly to about 600. Note that some of these particles do get trapped at the knee, some are carried away by the airflow and hence the number appears to be decreasing after about 25 seconds . From the instantaneous snapshot of the squames shown in Figure 8B,D, it can be seen
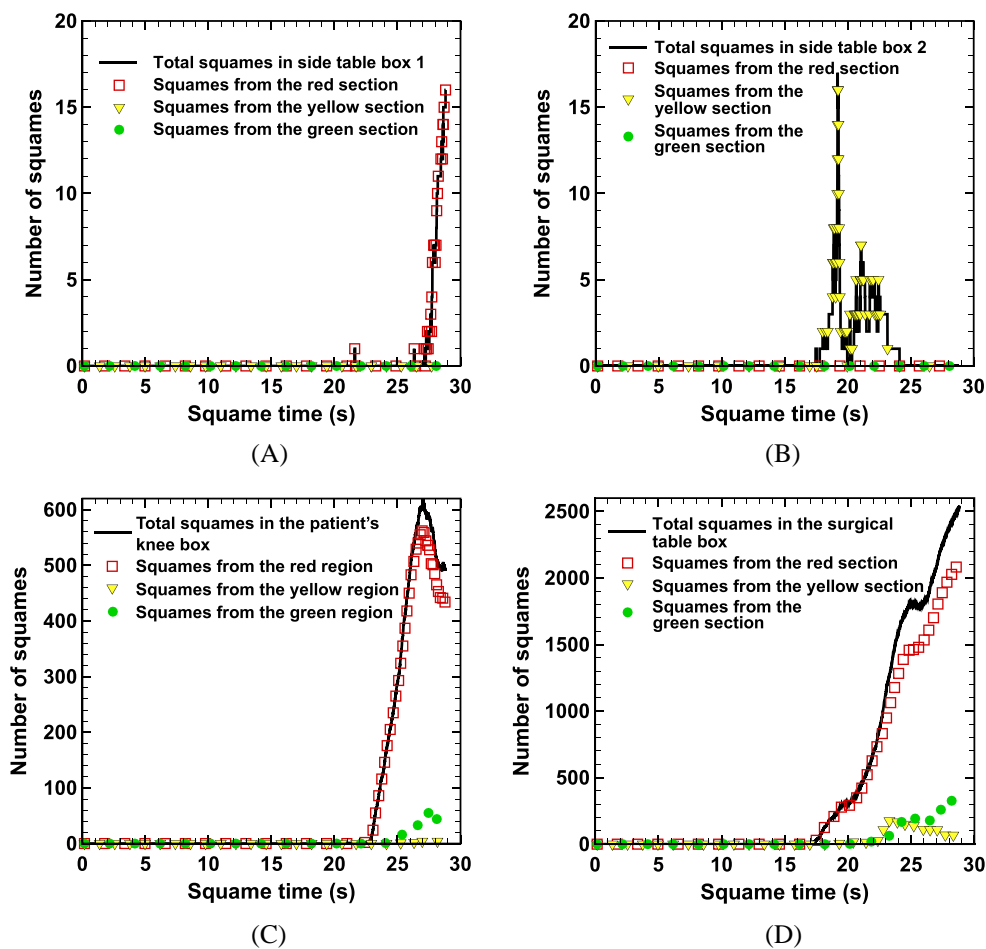

FIGURE 10 Temporal history of the total number of squames (shown by black color) entering 4 different regions of interest: A, Side table box 1. B, Side table box 2. C, The patient's knee area. D, The operating table box. Also shown in color is the number of color-coded squame particles entering from the red, green, and yellow regions

that several particles are still above the OT and moving downward due to the air from the inlet grilles. It is thus expected that more particles will enter the box above the patient's knee, potentially raising the probability of infection. It is also interesting to note that the squame particles entering the box above the OT and above the knee are mainly the red-colored particles initiated from the side of the OT with 2 surgeons. Owing to the asymmetry in the CAD model geometry, the flow pattern around each side of the OT is different and the recirculation region created by the incoming air from the inlet grilles is also asymmetric. The rise and eventual trapping of the squames within the knee box is thus also related to which side of the OT they originated from. The boxes above the side tables also entrain about 15 squame particles as can be seen from Figure 10A,B. This suggests that the surgical instruments on the side tables also have a small probability of carrying squames to the surgical site.

4 | SUMMARY AND CONCLUSION

A high-fidelity, LES was performed to study the interaction of the OR UCV airflow with the flow created by a forced air warming system (3M Bair Hugger blower) and the effect of this interaction on the dispersion of squames. A full three-dimensional CAD of an OR with OT, surgical lamps, medical staff, side tables, a blower, and a patient undergoing knee surgery was constructed. Unstructured grid elements involving hexahedra, tetrahedra, pyramids, and wedges were used to capture the complex geometry of the OR. An arbirary shaped, unstructured grid flow solver for LES based on governing equations for variable density in the limit of zero-Mach number was used. Ultra-clean ventilation air enters the OR through 10 ceiling grilles with 24.45 ACH and flow Reynolds number, based on the air inlet grille size and mean air inlet velocity, of 9226. The air inlet flow was developed from a periodic duct flow with the required target mass flow rate for each grille. No-slip boundary conditions were applied for all solid surfaces, and convective outflow condition was used at the 4 outlet grilles. Temperature values were prescribed at the surfaces of the inlet grilles, the surgical lamps, heads of the medical staff, patient's head, and patient's knee. All other boundary surfaces were assumed adiabatic. Computations were performed on 1600 processors in parallel and flow statistics involving the time-averaged mean velocity field, turbulence intensity, and temperature distribution were computed. Two computations were performed with the blower-off and blower-on to calculate a three-dimensional, time-dependent flow within the OR. Rising thermal plumes from the warm surfaces of surgeons heads, the patient's knee, patient's head, and the surgical lamp were calculated. With the blower on, air was drawn from the floor of the OR, heated, and blown into a blanket that covers the torso region of the patient. The blanket was covered with a plastic drape. The blower hot air generated forced convective currents and strong thermal plumes that interacted with the UCV air. For both cases, trajectories of 3 million squames, placed initially on the floor in a small region surrounding the OT and surgeons, were calculated and contrasted to quantify the effect of the hot air blower. The squames were assumed spherical in shape with 10 μm diameter and density of liquid water. The particle trajectories were tracked in a Lagrangian frame by computing the drag, lift, and buoyancy forces. The temporal variations of the number of squames within 4 imaginary boxes placed strategically above the 2 side tables, over the OT, and one surrounding the patient's knee were calculated and contrasted between the blower-off and blower-on cases. The following main conclusions can be drawn from these predictive computations:

1. For the **case of blower-off**, the ventilation air from the ceiling inlet grilles moves downwards, then is deflected by the surgical lights and the OT, impinges on the floor farther away from the OT, and finally exits through the outlet grilles. Large recirculation regions are created on both sides of the OT. The flow is not symmetric owing to asymmetries in the configuration of the OR contents. The maximum turbulence intensity level is about 30% in the high shear regions between the inlet air streams and the initial stagnant air in the OR, as well as near the warm surgical lights due to the buoyant plume. It is observed that the buoyant plumes from the patient's knee and other warm surfaces are relatively weak and do not significantly alter the mean ventilation airflow.
2. For the **case of blower-on**, the mean flow underneath and around the OT is significantly modified and large levels of turbulence intensity are observed under the OT. The turbulence intensity levels reach 60% in regions affected by the rising thermal plumes caused by the blower heated air. The instantaneous temperature contours confirm that the increased turbulence level is mainly due to the thermal plumes created by the hot blower air, thus raising the temperature regions under the OT in comparison with the blower-off case. The rising thermal plumes are observed to reach the ceiling in some regions.

3. The squames trajectories are significantly altered by turning the blower-on as compared to blower-off. With the blower-off, the majority of the squames are dispersed by the ventilation airflow towards the outlet grilles. None of the squames actually rise to the level of the side tables or the OT. In contrast, with the blower-on, a large number of squames are lifted upwards by the rising thermal plumes. Some of the squames are lifted above the surgeons heads and are blown towards the OT by the downward moving ventilation air. Large number of squames are seen to be above the OT, several are surrounding the surgeons hands, above the side tables, and some are very close to the patient's knee and the surgical site. Majority of the squames that come close to the surgical site were found to have originated from the sides parallel to the long side of the OT.

4. With the blower-off, none of the squames were found to enter the 4 imaginary boxes placed above the side tables, OT, and a region surrounding the patient's knee. Some particles are lifted from the floor over time, but none rise close to the level of the imaginary boxes as the downward flow due to the ventilation air keeps the particles closer to the floor. With the blower turned on, hot air discharged from the drape edges and the resultant thermal plumes drag the squames upwards. Some of the squames rise above the surgeons heads in the recirculation region on the sides of the OT. These particles are then flushed down onto the OT by the ventilation air from the inlet grilles. Statistically significant particles do enter the imaginary boxes of interest above the OT and the patient's knee. Few particles are also observed above the side tables.

Starting with the squames on the floor, it was shown that the hot air from the blower and the resultant thermal plumes are capable of lifting the particles and transporting them to the side tables, above the OT, and the surgical site. Motion of the medical staff, reaching for the surgical instruments placed on the side tables, and having suspended squames shed by the surgeons in the OR, can further enhance the probability of dispersing them to the surgical site. Although computationally intensive, LES of convective ventilation airflow and hot air from the blower in an OR is necessary to provide reliable predictions of the turbulent flow and dispersion of squames.

Limitations: In the present study, several other complexities involving other medical equipment in an OR, motion of the medical staff, opening and closing of the OR door, among others are not accounted for. However, these complexities may not impact the main conclusions of the present study.

The numerical approach used here is fully predictive and lacks any limitations from a theoretical point of view. However, there is lack of detailed experimental measurements of the three-dimensional velocity field in an OR during a clinical trial, which is emphasis of the "Reducing implant infection in orthopaedics (RIIiO) pilot study."[47] Such data would help validate the numerical predictions. Detailed flow measurements using three-component, PIV is needed that can provide high resolution data on mean and root mean square velocity fields. In addition, thermocouple measurements characterizing the temperature field in the OR are necessary. According to experts in fluid flow measurements, such detailed data during a clinical trial are potentially feasible but may cost up to $ 2 M.[48]

CONFLICT OF INTEREST

Authors have no conflicts of interest to declare.

ORCID

S. V. Apte http://orcid.org/0000-0002-3359-324X

REFERENCES

1. Clark RP, de Calcina-Goff ML. Some aspects of the airborne transmission of infection. *J R Soc Interface*. 2009;6(Suppl 6):S767-S782.
2. Wood A, Moss C, Keenan A, Reed M, Leaper DJ. Infection control hazards associated with the use of forced-air warming in operating theatres. *J Hosp Infect*. 2014;88(3):132-140.
3. Noble W, Lidwell O, Kingston D, et al. The size distribution of airborne particles carrying micro-organisms. *J Hyg (Lond)*. 1963;61(4):385-391.
4. Lees J, Brighton W. Simulated human skin scales. *J Hyg*. 1972;70(03):557-565.
5. Lidwell OM, Lowbury EJ, Whyte W, Blowers R, Stanley SJ, Lowe D. Effect of ultraclean air in operating rooms on deep sepsis in the joint after total hip or knee replacement: a randomised study. *BMJ*. 1982;285(6334):10-14.
6. Legg A, Cannon T, Hamer A. Do forced air patient-warming devices disrupt unidirectional downward airflow? *J Bone Joint Surg Br*. 2012;94(2):254-256.

7. McGovern P, Albrecht M, Belani K, et al. Forced-air warming and ultra-clean ventilation do not mix. *J Bone Joint Surg Br*. 2011;93(11):1537-1544.

8. Memarzadeh F, Manning AP. Comparison of operating room ventilation systems in the protection of the surgical site/discussion. *ASHRAE Trans*. 2002;108:1-13.

9. Pereira ML, Tribess A. A review of air distribution patterns in surgery rooms under infection control focus. *Rev Engenharia Térmica*. 2005;4(2):113-121.

10. Weinstein RA, Bonten MJM. Laminar airflow and surgical site infections: the evidence is blowing in the wind. *Lancet Infect Dis*. 2017;17(5):472-473.

11. Bischoff P, Kubilay NZ, Allegranzi B, Egger M, Gastmeier P. Effect of laminar airflow ventilation on surgical site infections: a systematic review and meta-analysis. *Lancet Infect Dis*. 2017;17(5):553-561.

12. Albrecht M, Gauthier RL, Belani K, Litchy M, Leaper D. Forced-air warming blowers: an evaluation of filtration adequacy and airborne contamination emissions in the operating room. *Am J Infect Control*. 2011;39(4):321-328.

13. Leaper D, Albrecht M, Gauthier R. Forced-air warming: a source of airborne contamination in the operating room? *Orthopedic Rev*. 2009;1(2):85-89.

14. Moretti B, Larocca A, Napoli C, et al. Active warming systems to maintain perioperative normothermia in hip replacement surgery: a therapeutic aid or a vector of infection? *J Hosp Infect*. 2009;73(1):58-63.

15. Sessler DI, Olmsted RN, Kuelpmann R. Forced-air warming does not worsen air quality in laminar flow operating rooms. *Anesth Analg*. 2011;113(6):1416-1421.

16. Sessler DI. Perioperative thermoregulation and heat balance. *The Lancet*. 2016;387(10038):2655-2664.

17. Dasari KB, Albrecht M, Harper M. Effect of forced-air warming on the performance of operating theatre laminar flow ventilation. *Anaesthesia*. 2012;67(3):244-249.

18. McNeill JS et al. Field measurements of thermal conditions during surgical procedures for the development of CFD boundary conditions. *ASHRAE Trans*. 2012;118:596-609.

19. McNeill J, Hertzberg J, Zhai ZJ. Experimental investigation of operating room air distribution in a full-scale laboratory chamber using particle image velocimetry and flow visualization; 2013.

20. Pope SB. *Turbulent Flows*. New York: Cambridge University Press; 2000.

21. Memarzadeh F. Reducing risks of surgery. *ASHRAE J*. 2003;45(2):28-33.

22. Chow TT, Wang J. Dynamic simulation on impact of surgeon bending movement on bacteria-carrying particles distribution in operating theatre. *Build Environ*. 2012;57:68-80.

23. Sommerfeld M, Ando A, Wennerberg D. Swirling, particle-laden flows through a pipe expansion. *J Fluids Eng*. 1992;114(4):648-656.

24. Chen XQ, Pereira J. Computation of particle dispersion in turbulent liquid flows using an efficient lagrangian trajectory model. *Int J Numer Methods Fluids*. 1998;26(3):345-364.

25. Piomelli U. Large eddy simulations in 2030 and beyond. *Philos Trans R Soc London A: Math, Phys Eng Sci*. 2014;372(2022): 20130320-20130320.

26. Apte S, Mahesh K, Moin P, Oefelein J. Large-eddy simulation of swirling particle-laden flows in a coaxial-jet combustor. *Int J Multiphase Flow*. 2003;29(8):1311-1331.

27. Moin P, Apte S. Large-eddy simulation of realistic gas turbine combustors. *AIAA J*. 2006;44(4):698-708.

28. Apte SV, Mahesh K, Gorokhovski M, Moin P. Stochastic modeling of atomizing spray in a complex swirl injector using large eddy simulation. *Proc Combust Inst*. 2009;32(2):2257-2266.

29. Mahesh K, Constantinescu G, Apte S, Iaccarino G, Ham F, Moin P. Large-eddy simulation of reacting turbulent flows in complex geometries. *J Appl Mech*. 2006;73:374-381.

30. Saarinen PE, Kalliomäki P, Tang JW, Koskela H. Large eddy simulation of air escape through a hospital isolation room single hinged doorwayvalidation by using tracer gases and simulated smoke videos. *PloS One*. 2015;10(7):1-19.

31. Moin P, Squires K, Cabot W, Lee S. A dynamic subgrid model for compressible turbulence and scalar transport. *Phys Fluids A*. 1991;3:2746-2757.

32. Germano M, Piomelli U, Moin P, Cabot WH. A dynamic subgrid-scale eddy viscosity model. *Phys Fluids A: Fluid Dyn (1989-1993)*. 1991;3(7):1760-1765.

33. Snyder OP. A 'Safe Hands' hand wash program for retail food operations: a technical review. *Yeast*. 2009;55(18.5):14-8.

34. Elghobashi SE. On predicting particle-laden turbulent flows. *J Applied Scientific Research*. 1994;52(4):309-329.

35. Maxey MR, Riley JJ. Equation of motion for a small rigid sphere in a nonuniform flow. *Phys Fluids (1958-1988)*. 1983;26(4):883-889.

36. Crowe C, Troutt T, Chung J. Numerical models for two-phase turbulent flows. *Annu Rev Fluid Mech*. 1996;28(1):11-43.

37. Saffman P. The lift on a small sphere in a slow shear flow. *J Fluid Mech*. 1965;22(02):385-400.

38. Finn J, Apte SV. Relative performance of body fitted and fictitious domain simulations of flow through fixed packed beds of spheres. *Int J Multiphase Flow*. 2013;56:54-71.

39. Mahesh K, Constantinescu G, Moin P. A numerical method for large-eddy simulation in complex geometries. *J Comput Phys*. 2004;197(1):215-240.

40. Ham F, Apte S, Iaccarino G, et al. Unstructured LES of reacting multiphase flows in realistic gas turbine combustors. Annual Research Briefs 2003. *Center Turbul Res, NASA Ames/Stanford Univ*. 2003:139-160.

41. Apte S, Gorokhovski M, Moin P. LES of atomizing spray with stochastic modeling of secondary breakup. *Int J Multiphase Flow*. 2003;29(9):1503-1522.

42. Apte S, Mahesh K, Lundgren T. Accounting for finite-size effects in simulations of disperse particle-laden flows. *Int J Multiphase Flow*. 2008;34(3):260-271.

43. Apte S, Mahesh K, Moin P. Large–eddy simulation of evaporating spray in a coaxial combustor. *Proc Combust Inst*. 2008;32:2247-2256.

44. Shams E, Apte SV. Prediction of small-scale cavitation in a high speed flow over an open cavity using large-eddy simulation. *J Fluids Eng*. 2010;132:11-14.

45. Shams E, Finn J, Apte SV. A numerical scheme for Euler-Lagrange simulation of bubbly flows in complex systems. *Int J Numer Methods Fluids*. 2010;67:1865-1898. https://doi.org/10.1002/fld.2452.

46. Pierce CD, Moin P. Large eddy simulation of a confined coaxial jet with swirl and heat release. *AIAA Pap*. 1998;2892.

47. Scarborough M. Reducing implant infection in orthopaedics (RIIiO) pilot study. 2017. https://doi.org/10.1186/isrctn74612906

48. Gharib M. Caltech, private communication; 2017.

49. Pierce CD. Progress-variable approach for large-eddy simulation of turbulent combustion. *Ph.D. Thesis*: Standford University, Palo, Alto, CA: Citeseer; 2001.

SUPPORTING INFORMATION

Additional Supporting Information may be found online in the supporting information tab for this article.

APPENDIX A

A.1 | Computational grid

For the present study, a computational mesh was generated using the CAD model described earlier to facilitate predictive large-eddy simulations. The mesh was generated using both tetrahedral and hexahedral cells. The transition of mesh from tetrahedral cells to hexahedral cells was done using a combination of pyramid and wedge-type cells. Care was taken to generate a computational grid that minimizes the grid skewness as much as possible. As shown below, in the regions away from the complex OR configuration involving the surgeons, the tables, the patient, and the drape, a mostly hex-dominant mesh is used. As one approaches closer to the operating table, the computational grid is transitioned to a predominantly tetrahedra-based mesh. The total mesh count for the computational domain is about 66 million.

Figure A1 shows the grid resolution near the air inlet cross-sections. The grid is appropriately refined to capture the shear layer generated by the inlet flow between the grilles. The mesh surrounding the OR table, patient, surgeons, side tables, the blower, and surgical lamps is predominantly tetrahedral. The tetrahedral mesh was carefully refined to capture surface curvature. Extra refinement was performed near surfaces which were in close proximity to other surfaces. This enhanced mesh refinement is to ensures that the effect of surface shapes on the flow and particles going around them will be captured by the simulation (Figure A2A,B)

As is shown in the above figures, a high-quality mesh was generated for the present LES investigation. Figure A3A shows histogram plot of cell skewness in the mesh. The average skewness was 0.14 and with maximum skewness was 0.91. Only 0.018% of cells had total skewness greater than 0.8 indicating the high quality of cells in the mesh. Another mesh metric that was checked was the aspect ratio of cells. The maximum aspect ratio was 16.2 and the average cell aspect ratio was 2.9, which indicate that a majority of cells in the mesh were mostly uniform (see Figure A3B).

A.2 | Computational algorithm

The numerical scheme for the solution of low-Mach number variable density flows on unstructured, arbitrary-shaped elements is based on the algorithms developed by coworkers.[27,29] A semi-implicit scheme is used for the fluid solver. For simplicity and readability, the notation used for filtered quantities in the LES formulation is dropped in this section. Also, the subscript g for gas-phase is dropped.

Figure A4 shows the schematic of variable storage in time and space. The Cartesian components of momentum, density, and pressure are stored at the centroids of the computational elements, and the face-normal velocity is stored at the centroids of the faces. The face-normal velocity is used to enforce continuity equation. We follow the collocated spatial
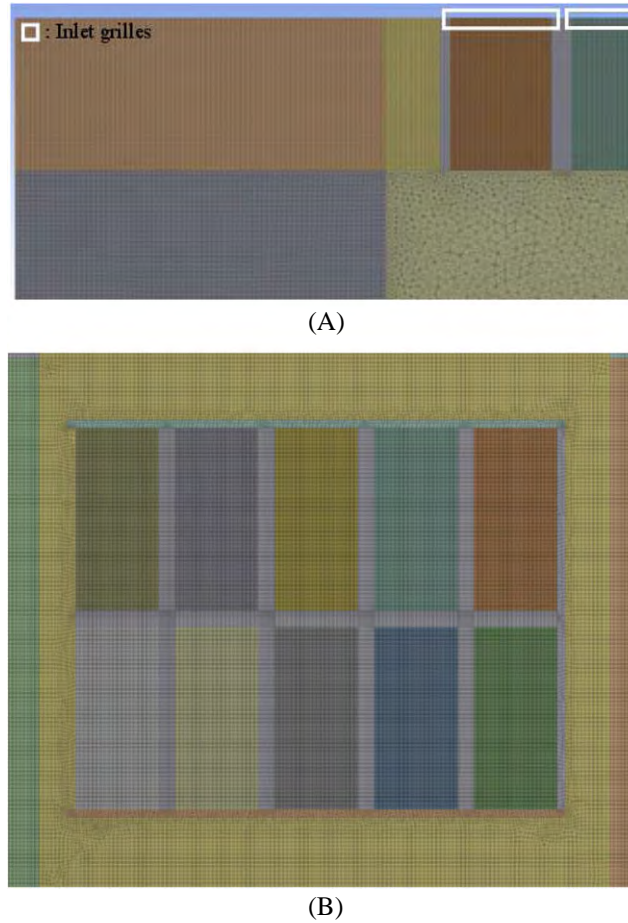
FIGURE A1 A cross section cut showing fine mesh near the ceiling of the room: A, Top view zoom-in. B, Top view showing all air inlet grilles

arrangement for velocity and pressure field. The main reason to use this arrangement as opposed to spatial-staggering is its easy application to unstructured grids and/or adaptive mesh refinement. The time-staggering is done so that the variables are located most conveniently for the time-advancement scheme. Accordingly, the density(ρ), specific enthalpy h, viscosity (μ), and thermal diffusivity (α) are located at time level $t^{n+1/2}$ and $t^{n+3/2}$ whereas the fluid velocity (u_i, u_N), and the pressure (p) are located at time level t^n and t^{n+1}. This makes the discretization symmetric in time, a feature important to obtain good conservation properties of the numerical scheme as emphasized and used by Pierce[49] for low-Mach number, reactive flows.

Using these variable locations, integrating the governing equations over the control volume and applying Gauss' divergence theorem to transport volume integrals to surface integrals wherever possible, the discrete governing equations are derived. Accordingly, the continuity equation is

$$\frac{\rho_{cv}^{n+3/2} - \rho_{cv}^{n+1/2}}{\Delta t} + \frac{1}{V_{cv}} \sum_{\text{faces of cv}} \rho_{cv}^{n+1} u_N^{n+1} A_{\text{face}} = 0, \tag{A1}$$

where ρ_{cv} is the density at the CV-center, Δt is the flow solver time-step, V_{cv} is the volume of the CV, A_{face} is the area of the face of a CV, u_N is the face-normal velocity, and ρ_{face} is the density at face of a CV. The density at the face can be readily obtained by using the arithmetic averages of the densities of the adjacent CVs (see Figure A4), that is, $\rho_{\text{face}} = \frac{1}{2}(\rho_{cv1} + \rho_{cv2})$. However, for the present colocated grid finite volume scheme the critical difference between the density and the face-normal velocity is that the face-normal velocity u_N is obtained through a projection scheme rather than interpolation. Furthermore, the density at time level t^{n+1} is also obtained from interpolation, $\rho_{\text{face}}^{n+1} = (\rho_{\text{face}}^{n+3/2} + \rho_{\text{face}}^{n+1/3})/2$.
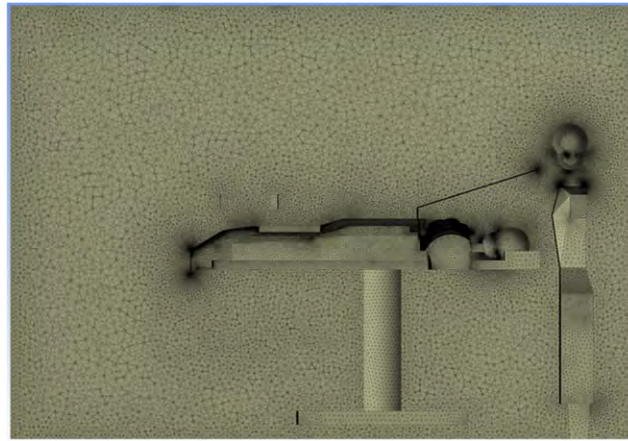
(A)
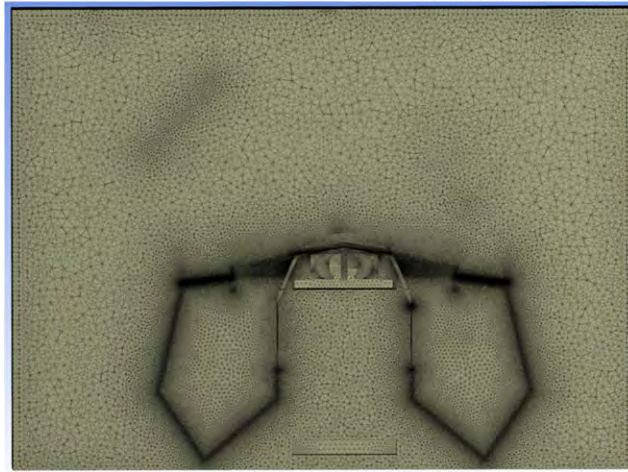
(B)

FIGURE A2   Mesh refinement near curved surfaces and surfaces that are in close proximity to others: A, Side view showing the entire operating table. B, Side view showing drapes

The discrete momentum equation for the ith component of velocity can be written as

$$\frac{g_{i,cv}^{n+1} - g_{i,cv}^{n}}{\Delta t} + \frac{1}{V_{cv}} \sum_{\text{faces of cv}} g_{i,\text{face}}^{n+1/2} u_{N}^{n+1/2} A_{\text{face}} = -\frac{\partial}{\partial x_i} p_{cv}^{n+1}$$
$$+ \frac{1}{V_{cv}} \sum_{\text{faces of cv}} \left(\tau_{ij}\right)_{\text{face}}^{n+1/2} N_{j,\text{face}} A_{\text{face}} + f_{i,cv}^{n+1/2}, \tag{A2}$$

where $g_i = \rho u_i$ represents the momentum in the ith direction, $(\tau_{ij})_{\text{face}}$ is the viscous stress at the faces of control volume, and $N_{j,\text{face}}$ represents the components of the outward face-normal. Similarly to the face density (ρ_{face}), the velocity field ($u_{i,\text{face}}$), and the momentum $\rho u_{i,\text{face}}$ at the faces are obtained using arithmetic averages of the corresponding fields at 2 control volumes associated with the face. The values at time level $t^{n+1/2}$ are obtained by time-averaging. The interface coupling force is represented by $f_{i,cv}$. The pressure field p_{cv}^{n+1} is unknown and is obtained using the best available guess at the current iteration. This gets updated during the solution of the pressure Poisson equation. The above discretization is implicit and thus the time-steps are not limited by viscous stability limits. The use of symmetric centered differences in space and time makes the algorithm second order on uniform Cartesian grids. The temperature field is obtained by the solution of the specific enthalpy equation. The above formulation handles variations in the fluid density (due to say temperature variations in a gaseous fluid) by relating the fluid density ρ to the temperature field through the ideal gas law. Note that once density is obtained the continuity equation can be imposed as a constraint on the momentum field, with the time-derivative of density as a source term. This constraint is enforced by the pressure, in a manner analogous to the enforcement of the incompressibility constraint for constant density flows.

Mesh Skewness

(A)
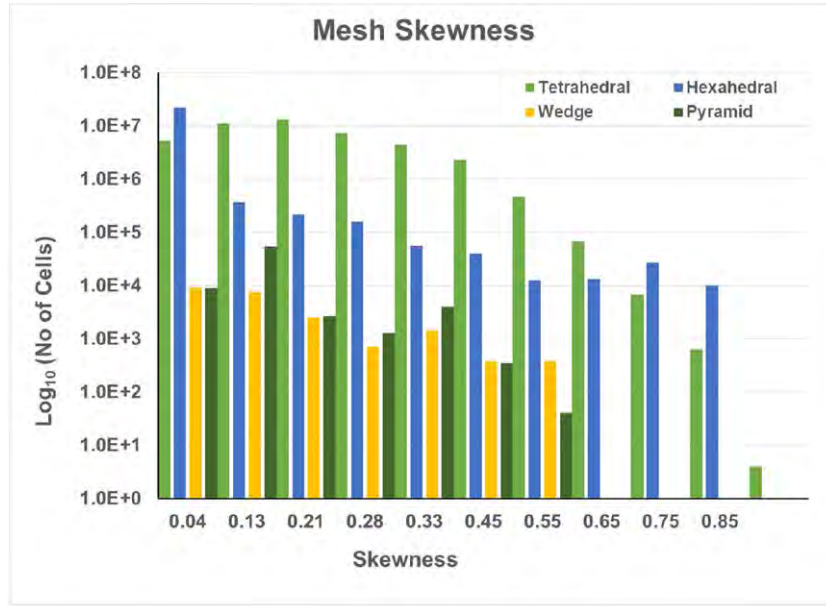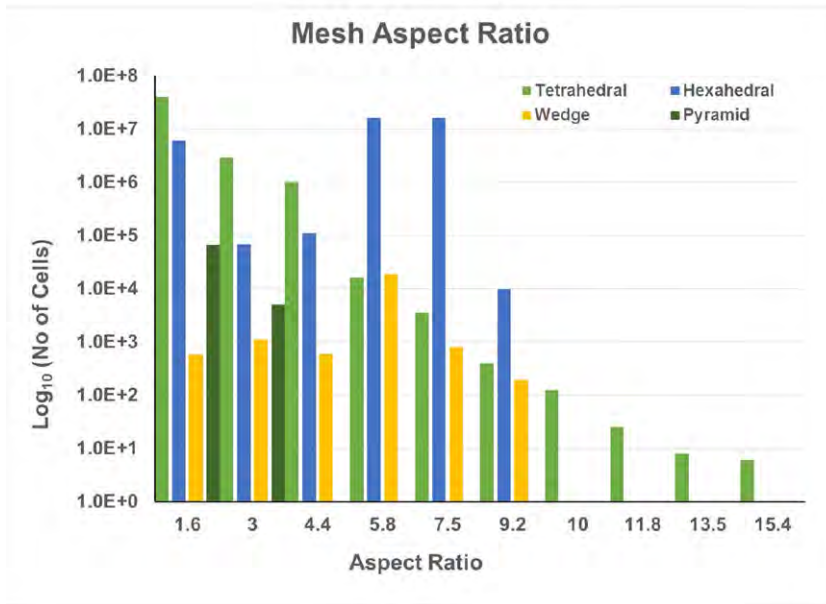
Mesh Aspect Ratio

(B)

FIGURE A3 Statistics histograms of the quality of mesh used in the computation: A, Skewness. B, Aspect ratio

The main steps of the solver are described below.

- **Step 1:** The specific enthalpy equation is first solved by using a third-order weighted essentially nonoscillatory (WENO) scheme for the advection term and central discretization for the diffusion term to obtain $h_{cv}^{n+3/2}$. The temperature is then calculated and density updated using the ideal gas law.
- **Step 2:** Advance the fluid momentum equations using the fractional step algorithm.

$$\frac{\rho_{cv}^{n+1}u_i^* - \rho_{cv}^n u_i^n}{\Delta t} + \frac{1}{2V_{cv}} \sum_{\text{faces of cv}} \left[\rho_{\text{face}}^{n+1}u_{i,\text{face}}^* + \rho_{\text{face}}^n u_{i,\text{face}}^n \right] u_N^{n+1/2} A_{\text{face}}$$

$$= -\frac{\delta p^n}{\delta x_i} + \frac{1}{2V_{cv}} \sum_{\text{faces of cv}} \mu_{\text{face}}^* \left(\frac{\partial u_{i,\text{face}}^*}{\partial x_j} + \frac{\partial u_{j,\text{face}}^n}{\partial x_i} \right) A_{\text{face}},$$
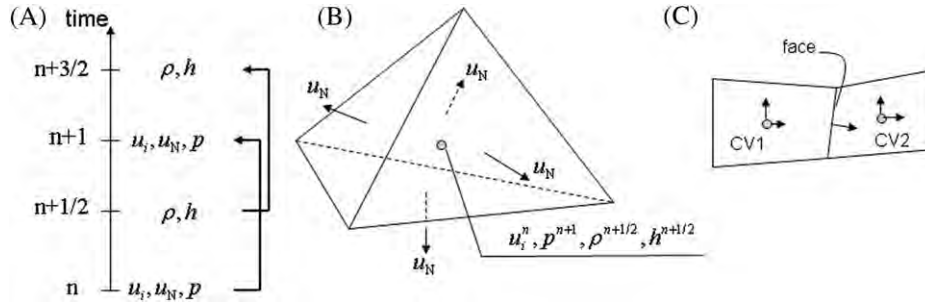
(A3)

FIGURE A4 Schematic of the grid stencil: A, Time staggering of variables. B, Velocity (u_i) and pressure fields (p) are colocated at the control volume center, u_N is the face-normal velocity. C, Control volume and face connectivity

where N is the face-normal component and A_{face} is the face area. The density fields at faces are obtained using simple arithmetic averages of density at adjacent CVs. Here, the fluid viscosity is given as μ^*_{face} and is the summation of the dynamic viscosity and eddy viscosity obtained from the dynamic Smagorinsky model. The pressure gradient at the CV centers in the above equation is at the old time-level and is obtained as described below. In the above step, the viscous terms are treated implicitly; the 3 equations for the velocity components at the CV centers are solved using iterative scheme such as Gauss-Seidel.

- **Step 3:** Remove the old pressure gradient to obtain the velocity field, $\widehat{u}_i$:

$$\frac{\rho^{n+1}_{\text{cv}}\widehat{u}_i - \rho^{n+1}_{\text{cv}}u^*_i}{\Delta t} = +\frac{\delta p}{\delta x_i}^n. \tag{A4}$$

- **Step 4:** Interpolate the velocity fields to the faces of the control volumes and consider the corrector step:

$$\frac{\rho^{n+1}_{\text{face}}u^{n+1}_N - \rho^{n+1}_{\text{face}}\widehat{u}_N}{\Delta t} = -\frac{\delta p}{\delta x_N}^{n+1}, \tag{A5}$$

where $\widehat{u}_N = \widehat{u}_{i,\text{face}}N_{i,\text{face}}$ is the approximation for face-normal velocity and $N_{i,\text{face}}$ are the components of the face-normal. To compute the face-based pressure gradient, we make use of the face and its 2 adjacent CVs (CV1 and CV2) as shown in Figure A4C. The face-normal pressure gradient is discretized as

$$\frac{\delta p}{\delta x_N}^{n+1} = \frac{p^{n+1}_{\text{nbr}} - p^{n+1}_{\text{cv}}}{|\mathbf{S}_{\text{cv}\to\text{nbr}}|}, \tag{A6}$$

where the subscripts CV and NBR stand for the the control volume CV for which the velocity field is being solved and the neighboring CV sharing a common face, respectively and $|\mathbf{S}_{\text{cv}\to\text{nbr}}|$ represents the magnitude of the vector connecting the 2 control volumes.

- **Step 5:** The pressure field and the pressure gradients at t^{n+1} are unknown in the above step. A pressure Poisson equation is derived by taking a discrete divergence of the above equations and solving for the pressure field at each control volume:

$$\sum_{\text{face of cv}} \Delta t \frac{\delta p}{\delta x_N}^{n+1} = \sum_{\text{faces of cv}} \rho^{n+1}_{\text{face}}\widehat{u}_{i,\text{face}}A_{\text{face}} + V_{\text{cv}}\frac{\rho^{n+3/2}_{\text{cv}} - \rho^{n+1/2}_{\text{cv}}}{\Delta t}. \tag{A7}$$

An algebraic multigrid approach is used to solve the Poisson system and is the most computationally intensive part of the algorithm per time-step.

- **Step 6:** Reconstruct the pressure gradient at the CV centers. The face-normal pressure gradient $\frac{\delta p}{\delta x_N}$ and the gradient in pressure at the CV-centroids are related by the area-weighted least-squares interpolation[29,39]:

$$\epsilon_{cv} = \sum_{\text{faces of cv}} \left(P'_{i,\text{cv}}N_{i,\text{face}} - P'_{\text{face}}\right)^2 A_{\text{face}}, \tag{A8}$$

where $P'_{i,\text{cv}} = \frac{\delta p}{\delta x_i}$ and $P'_{\text{face}} = \frac{\delta p}{\delta x_N}$.

- **Step 7:** Compute new face-based velocities, and update the CV-velocities:

$$u^{n+1}_N = \widehat{u}_N - \frac{\Delta t}{\rho^{n+1}_{\text{face}}}\frac{\delta p}{\delta x_N}^{n+1}, \tag{A9}$$

$$u^{n+1}_{i,\text{cv}} = \widehat{u}_{i,\text{cv}} - \frac{\Delta t}{\rho^{n+1}_{\text{cv}}}\frac{\delta p}{\delta x_{i,\text{cv}}}^{n+1}. \tag{A10}$$